

# Gradient-based optimization of exact stochastic kinetic models

Francesco Mottes,<sup>1,\*</sup> Qian-Ze Zhu,<sup>1</sup> and Michael P. Brenner<sup>1,†</sup>

<sup>1</sup>*School of Engineering and Applied Sciences, Harvard University, Cambridge MA 02138*

(Dated: January 21, 2026)

Stochastic kinetic models describe systems across biology, chemistry, and physics where discrete events and small populations render deterministic approximations inadequate. Parameter inference and inverse design in these systems require optimizing over trajectories generated by the Stochastic Simulation Algorithm, but the discrete reaction events involved are inherently non-differentiable. We present an approach based on straight-through Gumbel-Softmax estimation that maintains exact stochastic simulations in the forward pass while approximating gradients through a continuous relaxation applied only in the backward pass. We demonstrate robust performance on parameter inference in stochastic gene expression, accurately recovering kinetic rates of telegraph promoter models from both moment statistics and full steady-state distributions across diverse and challenging parameter regimes. We further demonstrate the method’s applicability to inverse design problems in stochastic thermodynamics, characterizing Pareto-optimal trade-offs between non-equilibrium currents and entropy production. The ability to efficiently differentiate through exact stochastic simulations provides a foundation for systematic inference and rational design across the many domains governed by continuous-time Markov dynamics.

## INTRODUCTION

Stochastic kinetic models, formalized as continuous-time Markov processes describing discrete state transitions, arise throughout the quantitative sciences. In systems biology, they are used to describe transcriptional bursting and regulatory switching underlying cell-to-cell variability in gene expression [1, 2]. Classic examples include the bistable lysis-lysogeny decision of lambda phage [3] and stochastic induction of the lac operon [4]. In non-equilibrium statistical mechanics, analogous frameworks describe molecular motors, driven transport processes, and the thermodynamic costs associated with maintaining currents far from equilibrium [5, 6]. In chemistry and ecology, stochastic kinetics govern reaction networks and population dynamics in regimes where small molecular counts and discrete events render deterministic approximations inadequate [7, 8].

The Chemical Master Equation (CME) provides the mathematical framework for describing the time evolution of probability distributions over discrete system states in stochastic kinetic models [9]. Analytical solutions, however, are available only for restricted classes of reaction networks [10, 11]. For general systems, exact sample trajectories can be generated using Gillespie’s Stochastic Simulation Algorithm (SSA) [12], which produces realizations of the underlying continuous-time Markov process. Parameter inference and inverse design in these systems therefore relies mostly on simulation-based approaches.

Solving inverse problems in stochastic kinetic systems is essential for extracting mechanistic insight from noisy experimental data, and substantial effort has been devoted to developing inference methods. For systems with

state spaces amenable to controlled truncation, Finite State Projection and related methods enable likelihood-based inference [13–16], but require explicit representation of the truncated state space. Moment-based methods offer computational efficiency, but only when low-order statistics are informative [17]. Bayesian frameworks, including Approximate Bayesian Computation [18, 19] and particle Markov chain Monte Carlo [20, 21], provide rigorous uncertainty quantification but can become computationally demanding in higher-dimensional parameter spaces. Gradient-based optimization is an attractive alternative, since reverse-mode automatic differentiation provides gradients at cost comparable to a single forward evaluation [22]. However, the discrete reaction selections and state updates in the SSA are intrinsically non-differentiable, precluding direct pathwise differentiation. Likelihood ratio estimators yield unbiased gradients without requiring differentiable dynamics [23, 24], but exhibit variance that grows with trajectory length. Finite difference methods provide an alternative, but their computational cost scales linearly with the number of parameters, even when using variance-reduction schemes that drastically improve convergence [25]. Recent work introduced a continuous SSA relaxation enabling end-to-end differentiation [26], though at the cost of approximation errors in forward dynamics that accumulate over trajectory length, propagate into gradient estimates, and break permutation symmetry across reaction channels.

Here we introduce a reparameterized gradient estimator that enables efficient optimization while maintaining exact stochastic simulations. The approach preserves full fidelity of the Chemical Master Equation, retaining discrete reaction events and correct waiting time statistics in forward trajectories, while providing low-variance gradient estimates compatible with modern adaptive optimizers. We achieve this through straight-through Gumbel-Softmax estimation [27, 28], decoupling forward sampling

\* fmottes@seas.harvard.edu

† brenner@seas.harvard.edu

from backward differentiation. In the forward pass, exact discrete samples are drawn according to the SSA. In the backward pass, gradients are propagated through a continuous relaxation of the categorical sampling operation. The resulting estimator exhibits substantially lower variance than likelihood ratio methods and avoids the approximation errors introduced by continuous relaxations of forward dynamics.

We demonstrate the framework on two problem classes spanning biophysics and non-equilibrium statistical mechanics. First, we address parameter inference in stochastic gene expression, recovering kinetic rates of telegraph promoter models from both moment statistics and full steady-state probability distributions. Using differentiable histogram construction, we show that distribution-level optimization accurately recovers ground-truth parameters across kinetic regimes characteristic of prokaryotic transcription. Second, we apply the method to optimization problems in stochastic thermodynamics, maximizing non-equilibrium currents under constraints on entropy production and kinetic resources. We characterize Pareto-optimal trade-offs between current magnitude and dissipation, recovering known theoretical bounds. These applications illustrate the generality of the approach: any scalar objective computable from stochastic trajectories becomes accessible to efficient gradient-based optimization.

## A REPARAMETERIZED PATHWISE GRADIENT ESTIMATOR

The Stochastic Simulation Algorithm involves two sampling operations at each step, selecting which reaction occurs and when it occurs (Fig. 1, left). Both can be written as deterministic functions of parameter-independent random draws, enabling gradients to flow through the simulation while preserving exact discrete dynamics (Fig. 1, right).

For waiting times, this reparameterization is standard. If  $u \sim \mathcal{U}(0, 1)$ , then  $\Delta t = -\log u/a_0(\theta)$  is exponentially distributed with rate equal to the total propensity  $a_0(\theta) = \sum_j a_j(\theta)$ . Since  $\Delta t$  is an explicit function of the propensities, gradients flow through the waiting time automatically. The categorical sampling of reaction identity appears more problematic, since selecting reaction index  $r$  with probability  $\pi_r = a_r/a_0$  requires a discrete choice. However, this too admits reparameterization through the Gumbel-Max trick. If  $u_k \sim \mathcal{U}(0, 1)$  are independent samples then  $g_k = -\log(-\log u_k)$  follow the standard Gumbel distribution, and

$$y = \text{one\_hot} \left( \arg \max_k (g_k + \log \pi_k) \right)$$

samples from the correct categorical distribution. Expressing the selected reaction as a one-hot vector allows the state update to be written as a matrix-vector product with the stoichiometry matrix. The discrete outcome

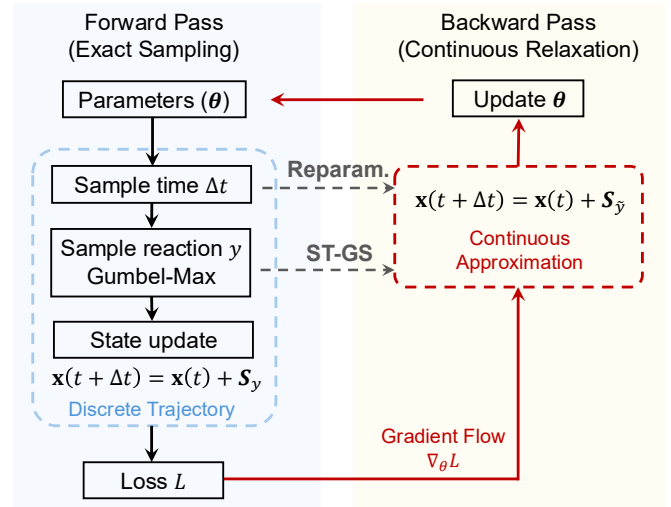


FIG. 1. **Modeling and Optimization Framework.** SSA trajectories are generated exactly in the forward pass by sampling waiting times and discrete reaction events (Left, blue shaded box). In the backward pass, gradients are computed by directly reparameterizing waiting times and applying a continuous Gumbel-Softmax relaxation to reaction selection (Right, yellow shaded box), enabling efficient gradient-based optimization without approximating the stochastic dynamics.

is now expressed as a deterministic function of fixed random inputs  $\{g_k\}$  and the parameter-dependent reaction propensities  $\{a_k(\theta)\}$ .

The Gumbel-Max formulation explicitly exposes the source of non-differentiability: the arg max operation has zero gradients almost everywhere. The *straight-through Gumbel-Softmax* (ST-GS) estimator resolves this by employing different operations for forward and backward passes [27, 28]. In the forward pass, we evaluate the exact arg max to obtain a discrete one-hot vector  $y$  specifying the selected reaction. In the backward pass, we substitute the softmax relaxation

$$\tilde{y}_k = \frac{\exp((g_k + \log \pi_k)/\tau)}{\sum_j \exp((g_j + \log \pi_j)/\tau)}$$

and backpropagate gradients through this continuous approximation. The temperature parameter  $\tau$  controls the fidelity of the approximation. As  $\tau \rightarrow 0$ , the softmax concentrates toward the arg max, reducing bias but increasing gradient variance. Larger values of  $\tau$  yield smoother gradients at the cost of a less accurate approximation to the true sensitivity. We find  $\tau = 1.0$  provides a robust default across the applications considered in this work.

The resulting gradient estimator is biased, since derivatives computed through the softmax relaxation do not necessarily equal the true sensitivity of the discrete system. However, the bias is confined to the gradient calculation. Every forward trajectory remains an exact sample from the Chemical Master Equation, ensuring that optimized parameters are evaluated against faithful stochastic dynamics. A more thorough derivation is provided in

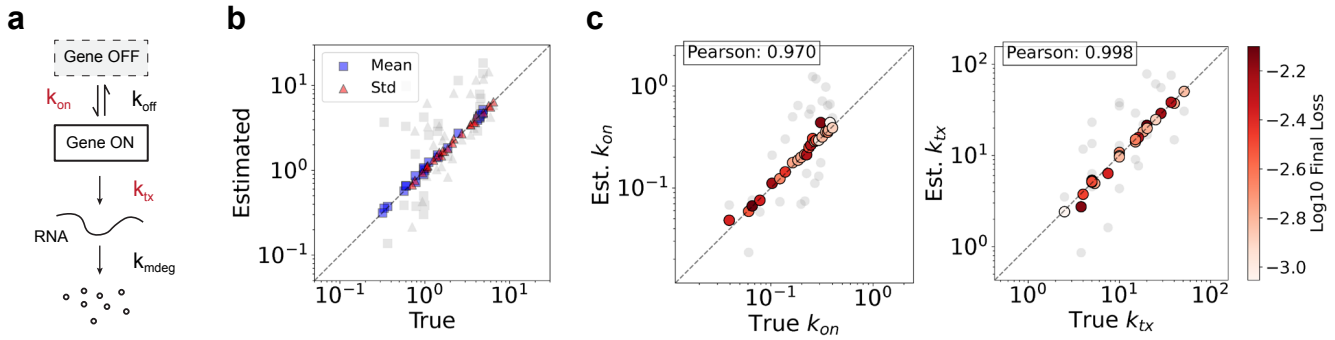


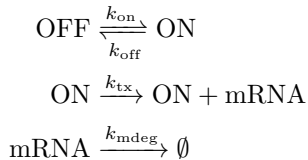
**FIG. 2. Moment matching inferences from synthetic data.** Inference of parameters from mean and variance of the true underlying generative model at steady state, for 25 different parameter sets. Gray markers indicate the random initializations. (a) Two parameters of the telegraph model ( $k_{\text{on}}$ ,  $k_{\text{tx}}$ ) are simultaneously estimated. (b) Mean and standard deviation of the RNA levels at steady state for the true and optimized models. (c) Comparison between the estimated and true rates.

Section S1.

### PARAMETER INFERENCE IN STOCHASTIC GENE EXPRESSION

We validate our inference framework on the telegraph promoter model, a canonical description of stochastic gene expression widely adopted in systems biology. First introduced by Peccoud and Ycart [29], the telegraph model has successfully explained experimental observations of transcriptional bursting across prokaryotic [30, 31] and eukaryotic systems [32, 33], and remains the basis for modern inference frameworks applied to single-cell RNA sequencing data [34].

The model describes a gene switching stochastically between two discrete promoter states: ON, permitting transcription, and OFF, where transcription is inhibited. The promoter transitions between states with rates  $k_{\text{on}}$  and  $k_{\text{off}}$ . In the ON state, mRNA is produced at rate  $k_{\text{tx}}$ , while mRNA degradation occurs at rate  $k_{\text{mdeg}}$ . The system is represented by three reactions:



We generate a diverse synthetic dataset by sampling 25 parameter sets from ranges consistent with bacterial transcriptional dynamics (*Methods*). For each parameter set, we simulate the stochastic process until steady state and record the resulting single-cell RNA count distribution. These distributions serve as input for inference, allowing direct comparison between inferred and ground-truth parameters. We restrict our analysis to parameter regimes where the model is structurally identifiable in theory, isolating the performance of the inference method from fundamental limitations of the model itself.

### Moment Matching

We first consider inferring two parameters of the telegraph model ( $k_{\text{on}}$  and  $k_{\text{tx}}$ ) while fixing the others to their ground-truth values (Fig. 2a). We initialize the free parameters randomly within a log-uniform range spanning  $[0.2 \times, 5 \times]$  their true values. With only two free parameters, matching the mean and variance of the stationary distribution uniquely determines the solution.

We minimize the following loss function:

$$\mathcal{L} = \left[ \log_{10} \left( \frac{\mu_{\text{true}}}{\mu_{\text{sim}}} \right) \right]^2 + \left[ \log_{10} \left( \frac{\sigma_{\text{true}}^2}{\sigma_{\text{sim}}^2} \right) \right]^2$$

where  $\mu_{\text{true}}, \sigma_{\text{true}}^2$  and  $\mu_{\text{sim}}, \sigma_{\text{sim}}^2$  are the mean and variance of the RNA copy number at steady state for the ground truth and simulated model, respectively. The logarithmic ratio formulation ensures that relative errors are penalized equally regardless of the absolute scale of each statistic. Rate constants are optimized in logarithmic space, enforcing positivity and normalizing sensitivity across parameters of different magnitudes.

The optimized models accurately reproduce target moments (Fig. 2b), and recovers the true values of  $k_{\text{on}}$  and  $k_{\text{tx}}$  across all 25 parameter sets (Fig. 2c). We note that a previous study using automatic differentiation (but without the current methodology) on this class of problems achieved Pearson correlations of 0.68–0.74 using less challenging parameter regimes [26]. Full results are reported in Fig. S1.

Despite its apparent simplicity, this problem presents non-trivial optimization challenges. Although it admits a unique and analytically derivable minimum, the loss landscape is severely ill-conditioned around the global optimum, owing to loss landscapes featuring flat ridges corresponding to directions of low sensitivity [35]. This poses significant challenges to first-order optimizers, even when using adaptive methods such as Adam [36]. Achieving full convergence required deviating from standard hyperparameter settings, as detailed in *Methods*. The

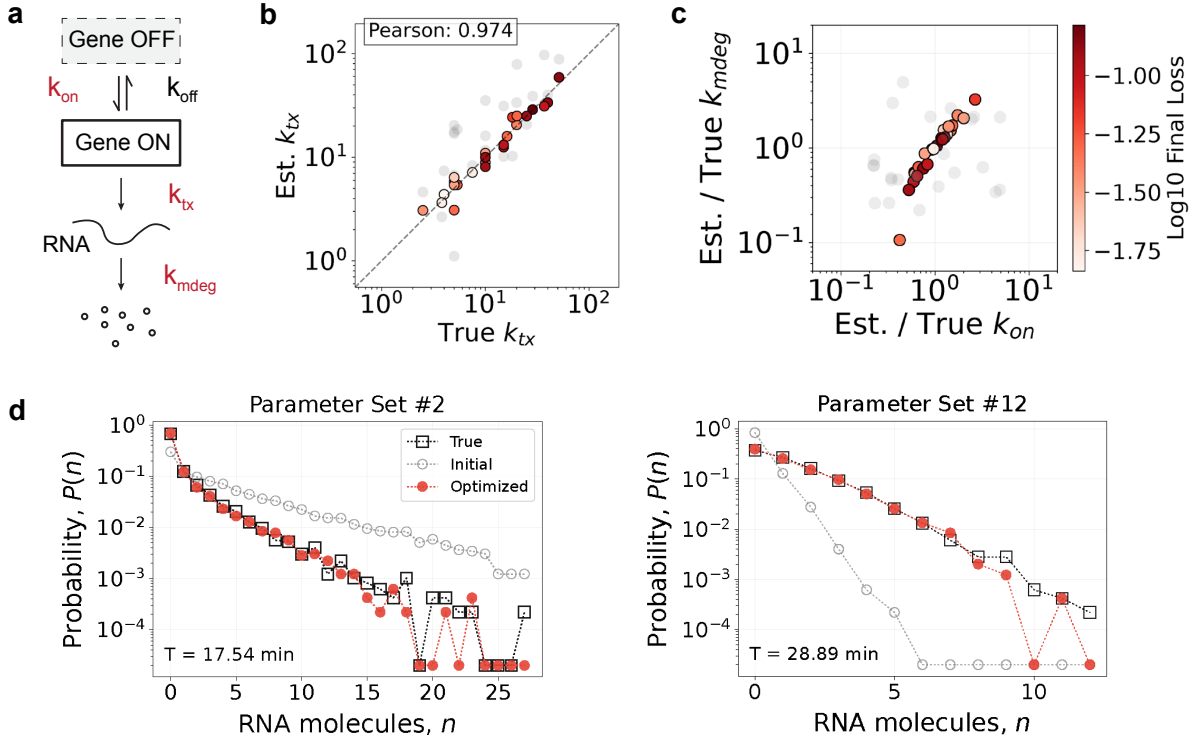


**FIG. 3. Distribution matching inferences from synthetic data.** Inference of parameters from the RNA histogram of the true underlying generative model at steady state, for 25 different parameter sets. Gray markers indicate the random initializations. (a) Three parameters of the telegraph model ( $k_{on}$ ,  $k_{tx}$ ,  $k_{mdeg}$ ) are simultaneously estimated. (b) Comparison between the estimated and true transcription rate. (c) Relative errors in the estimation of the degradation rate  $k_{mdeg}$  and the on-rate  $k_{on}$  illustrate sloppy parameters directions. (d) Two representative examples comparing the target data distribution (black) and the distribution generated by the optimized model (red), showing agreement over several orders of magnitude.

moment matching problem can be reformulated into a better-conditioned problem by reparameterizing to fit burst frequency  $k_{on}k_{off}/(k_{on} + k_{off})$  and mean burst size  $k_{tx}/k_{off}$ , effectively preconditioning the landscape. However, identifying such reparameterizations is generally non-trivial, and we demonstrate here that our method is sufficiently robust to solve the original ill-conditioned problem directly.

### Distribution Matching

We next consider inference from the full steady-state RNA copy-number distribution. The complete distribution contains substantially more information than moments alone and in principle can uniquely determine additional kinetic parameters. With three free parameters ( $k_{on}$ ,  $k_{tx}$ ,  $k_{mdeg}$ ) and the remaining rate fixed to its ground-truth value (Fig. 3a), the optimization problem admits a unique minimum. In practice, however, the loss landscape exhibits pronounced near-degeneracies: coupled changes in promoter switching and mRNA degradation can produce nearly indistinguishable steady-state distributions, making the global optimum difficult to lo-

cate numerically.

We quantify distributional mismatch using the 1-Wasserstein (Earth Mover's) distance, which for one-dimensional distributions can be calculated as the  $L_1$  distance between two cumulative distribution functions [37]:

$$\mathcal{L} = \sum_n |F_{\text{true}}(n) - F_{\text{sim}}(n)|,$$

where  $F_{\text{true}}$  and  $F_{\text{sim}}$  denote the empirical CDFs of the target and simulated RNA counts, respectively. Our experiments showed that this objective is more robust than the more common information-theoretic alternatives: cross-entropy and KL divergence underweight low-probability bins and therefore neglects the tails, while symmetric divergences such as Jensen-Shannon become numerically unstable.

Optimizing this loss requires differentiating through the simulated RNA histogram. For this we employ a triangular kernel density estimator with unit bandwidth. For integer-valued data, this produces histograms identical to standard hard binning, while providing well-defined gradients (*Methods*). Accurately resolving the distribution, particularly in the tails, requires a large number of simulations, but backpropagating through

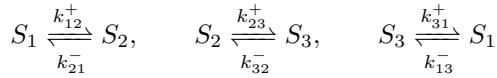
all of them would exceed even very loose memory constraints. We therefore compute distributional statistics from a large pool of forward-only simulations combined with a smaller set of gradient-tracked trajectories (*Methods*). This decouples the sample size needed for accurate distribution estimates from the memory cost of gradient computation, with the benefit of reducing gradient variance. Given the stiffness of this inverse problem, we adopt a multi-start protocol, running three independent optimizations from random initializations spanning  $[0.2\times, 5\times]$  the ground-truth values and reporting the solution with the lowest loss.

Across the 25 synthetic parameter sets, this procedure recovers  $k_{\text{tx}}$  accurately (Fig. 3b). The remaining parameters exhibit correlated deviations (Fig. 3c): errors in  $k_{\text{on}}$  and  $k_{\text{mdeg}}$  are anticorrelated, reflecting a near-degenerate direction in the loss landscape where changes in switching kinetics can be partially compensated by changes in degradation. This pattern is consistent with the “sloppy parameter” structure characteristic of kinetic models [35]. Importantly, despite the difficulty of pinpointing the unique optimum along this degenerate direction, the optimized models faithfully reproduce the full target distribution over several orders of magnitude in probability (Fig. 3d; full results in Figs. S5–S6). This demonstrates that ST-GS gradients provide sufficient signal to solve challenging distribution-level inverse problems while maintaining exact SSA dynamics throughout.

## CONSTRAINED OPTIMIZATION IN NONEQUILIBRIUM STOCHASTIC THERMODYNAMICS

We next apply our framework to an inverse design problem in stochastic thermodynamics [5]: characterizing the Pareto front of optimal trade-offs between steady-state current and entropy production in a driven system with fixed kinetic resources. This problem combines core ingredients of non-equilibrium thermodynamics (cycle currents, thermodynamic affinities, dissipation constraints) in a minimal setting that admits analytical solution, providing a rigorous benchmark.

We study a three-state ring [38] where a particle transitions cyclically among states  $S_1 \rightarrow S_2 \rightarrow S_3 \rightarrow S_1$ , with each edge supporting both forward and backward transitions (Fig. 4a):



When detailed balance is broken, a net cycle current  $J$  circulates through the ring. The thermodynamic cost of maintaining this current is the entropy production rate  $\sigma = J \cdot \mathcal{A}$ , where  $\mathcal{A} = \sum_i \log(k_i^+/k_i^-)$  is the cycle affinity [10]. We additionally impose a kinetic budget  $K_{\text{tot}} = \sum_i (k_i^+ + k_i^-)$ , which functions as a bound on the system’s dynamical activity [39].

The inverse design objective is to maximize  $J$  at fixed  $\sigma$  and  $K_{\text{tot}}$ . The exact cycle current (net reaction counts divided by time) is not differentiable with respect to rate parameters. We instead estimate the current from simulated trajectories as

$$\hat{J} = \frac{1}{3T} \sum_n \left[ \sum_i a_i^+(t_n) - \sum_i a_i^-(t_n) \right] \Delta t_n$$

where  $a_i^\pm(t_n)$  are the forward and backward propensities and  $\Delta t_n$  is the waiting time at step  $n$ . This time-weighted propensity average is differentiable and provides gradients with respect to all rate parameters. The entropy production estimate follows as  $\hat{\sigma} = \hat{J} \cdot \mathcal{A}$ . Since thermodynamic behavior depends on rate ratios  $k_i^+/k_i^-$ , the same physical driving can arise from many absolute rate values. We constrain all backward rates to a common value (still learnable given the fixed total budget), establishing a reference scale that removes this degeneracy and makes the optimized forward rates directly comparable across edges. Constraints are enforced through logarithmic penalties, ensuring scale-invariant treatment across the range of target values:

$$\mathcal{L} = -\hat{J} + \lambda_\sigma \left[ \log \frac{\hat{\sigma}}{\sigma_{\text{target}}} \right]^2 + \lambda_K \left[ \log \frac{K_{\text{tot}}}{K_{\text{target}}} \right]^2$$

We optimize across target entropy production values spanning two orders of magnitude ( $\sigma \in [0.01, 2.5]$ ). All optimizations start from the same random initial rates and are run to stable convergence using the modified Adam optimizer described in *Methods*.

For the symmetric ring with fixed kinetic budget  $K_{\text{tot}}$ , the Pareto-optimal current at affinity  $\mathcal{A}$  follows from steady-state analysis (Section S2):

$$J = \frac{K_{\text{tot}}}{9} \tanh \frac{\mathcal{A}}{6}, \quad \sigma = J\mathcal{A}$$

This defines a fundamental bound: no rate configuration with the given kinetic budget can achieve higher current at a given dissipation level.

The optimized cycle currents closely track the theoretical Pareto front across the full range of target dissipation values (Fig. 4b). Agreement extends from the near-equilibrium regime ( $\sigma \ll 1$ ), where  $J \propto \sqrt{\sigma}$  (dotted line) [40], to the far-from-equilibrium regime ( $\sigma \gtrsim 1$ ), where current saturates toward its maximum value  $J_{\text{max}} = K_{\text{tot}}/9$ . To assess constraint satisfaction, we evaluate relative errors in the optimized current (compared to the theoretical optimum), entropy production rate, and total kinetic budget (compared to their target values). The kinetic budget constraint is satisfied to within fractions of 1% across all runs (Fig. 4c, green triangles; Table S1), ensuring valid comparison with the theoretical bound. Relative errors in  $J$  and  $\sigma$  remain small throughout the moderate-to-high dissipation regime but increase at the lowest entropy production targets, where

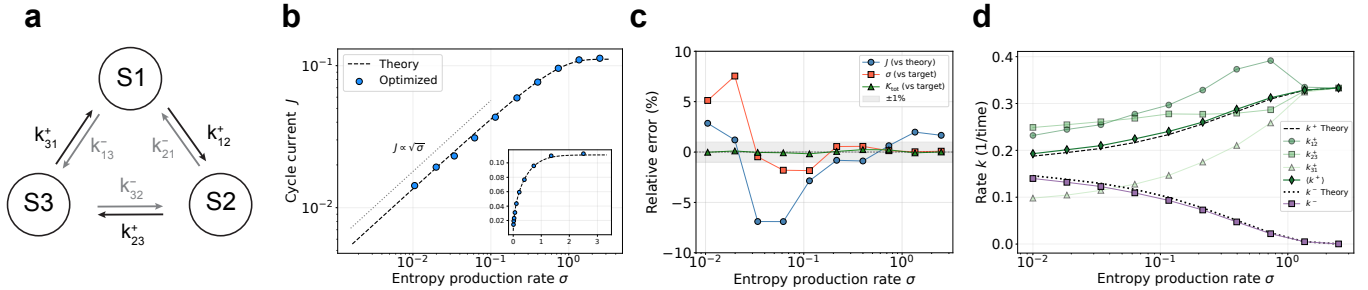


FIG. 4. **Optimal current-dissipation trade-off in a three-state ring.** Optimization of cycle current  $J$  under constraints on entropy production rate  $\sigma$  and total kinetic budget  $K_{\text{tot}}$ . (a) Schematic of the three-state ring with forward ( $k_{ij}^+$ ) and backward ( $k_{ji}^-$ ) transition rates. (b) Optimized cycle current (blue circles) compared to the theoretical Pareto front (dashed line). Dotted line: asymptotic near-equilibrium scaling. Inset: Pareto front on linear axes. (c) Relative errors in  $J$  (versus theory),  $\sigma$ , and  $K_{\text{tot}}$  (versus target). Shaded band:  $\pm 1\%$ . (d) Optimized forward rates  $k_{12}^+$ ,  $k_{23}^+$ ,  $k_{31}^+$  (light green symbols), their mean  $\langle k^+ \rangle$  (green diamonds), and backward rate  $k^-$  (squares), compared to theoretical predictions (dashed and dotted lines).

the near-equilibrium current becomes vanishingly small and stochastic fluctuations dominate.

The optimized common backward rate  $k^-$  and mean forward rate  $\langle k^+ \rangle$  closely follow theoretical predictions (Fig. 4d). The individual forward rates, instead, display substantial spread near equilibrium before converging to the fully symmetric allocation at high dissipation (Fig. 4d, light green symbols). This behavior is consistent with the close agreement between optimized currents and the Pareto bound: at small  $\sigma$ , the optimal rate configuration is only weakly determined at the level of individual edges. Many distinct allocations of the forward-rate budget yield indistinguishable  $J(\sigma)$  once  $\sigma$  and  $K_{\text{tot}}$  are fixed, producing a broad family of near-degenerate solutions. Physically, although the smallest forward rate would nominally act as a bottleneck, transitions in the near-equilibrium regime are so infrequent that the delay from a single slow edge becomes negligible compared to the long waiting times throughout the cycle. Far from equilibrium, cycles complete rapidly enough that any rate asymmetry creates a persistent bottleneck, reducing the attainable current and driving the system toward symmetric rate allocation. Detailed optimization trajectories for each target  $\sigma$  are provided in Figs. S10–S19.

These results establish the framework as a practical tool for rational design of non-equilibrium systems under thermodynamic constraints, capable of tracking optimal solutions across different constraints.

## DISCUSSION

The ST-GS estimator introduces a biased approximation to gradient computation, controlled by a single temperature hyperparameter  $\tau$ . Crucially, this bias affects only the backward pass, while forward trajectories remain exact samples from the Chemical Master Equation throughout optimization. While theoretical characterization of the bias remains an open question, we find that the default value  $\tau = 1$  yields sufficiently accurate gradi-

ents for precise parameter recovery across diverse kinetic regimes and close agreement with analytical predictions in the thermodynamic optimization problem. This suggests the approach is robust for practical applications without requiring problem-specific tuning.

Differentiability does not, however, eliminate the intrinsic difficulty of inverse problems in stochastic kinetic systems. The loss landscapes exhibit the flat ridges and sloppy parameter directions characteristic of kinetic models, requiring careful optimizer configuration. We deliberately avoided problem-specific manipulations such as reparameterizations to better-conditioned variables or non-dimensionalization schemes that, while potentially easing optimization, would obscure the general applicability of the method. Full convergence was nonetheless achieved using modified Adam hyperparameters. Second-order methods that account for local curvature may offer further improvements but are more susceptible to noise in stochastic gradient estimates. The feasibility of gradient-based optimization demonstrated here may motivate systematic study of loss landscape geometry in kinetic models and the design of inference algorithms tailored to this problem structure, paralleling historical developments in neural network optimization.

A principal motivation for gradient-based approaches is that reverse-mode automatic differentiation scales independently of parameter dimensionality, in principle enabling efficient inference in large mechanistic models. We have deliberately restricted this study to low-dimensional systems where analytical solutions or ground-truth parameters permit rigorous validation. Extending to higher-dimensional systems is a natural direction but will require addressing the compounding challenges of optimization in increasingly degenerate landscapes.

A significant limitation of this work is the absence of experimental data. Demonstrating robust inference on real gene expression measurements—subject to technical noise, incomplete detection, and biological heterogeneity—will be necessary to establish the practical utility

of this framework. Additionally, integration with variational inference methods such as ADVI could extend the approach to full posterior estimation, expanding the reach of Bayesian inference in biophysics and stochastic thermodynamics.

Finally, stochastic kinetic models extend well beyond the applications considered here, finding use in epidemiology, ecology, neuroscience, and the social sciences. The ability to efficiently differentiate through exact stochastic simulations provides a foundation for large-scale inference and principled investigation of optimality across the many domains governed by continuous-time Markov dynamics.

## METHODS

Fully differentiable, hardware-accelerated simulations were coded using the JAX python library [41] and other libraries in the JAX ecosystem, in particular Equinox [42] as the simulation backbone. JAX provides automatic differentiation, just-in-time compilation and automatic vectorization that greatly improve computational performance of Monte Carlo gradient estimation. We provide a succinct overview of the main components of our model. A full mathematical account of simulation and optimization details is given in the *Supplementary Information*.

### Synthetic Data

We generate 25 parameter sets  $\{k_{\text{on}}, k_{\text{off}}, k_{\text{tx}}, k_{\text{mdeg}}\}$  chosen to span a range of biologically plausible kinetic regimes characteristic of bacterial gene expression. The off-rate is fixed at  $k_{\text{off}} = 5.0 \text{ min}^{-1}$ , corresponding to a mean ON-state duration ( $1/k_{\text{off}}$ ) of approximately 12 seconds. This implies short transcriptional bursts, consistent with rapid transcription factor binding and unbinding dynamics. The mRNA degradation rate  $k_{\text{mdeg}}$  ranges from 0.12 to  $0.7 \text{ min}^{-1}$ , corresponding to half-lives of approximately 1–6 minutes. This range encompasses typical *E. coli* mRNA lifetimes, where the average half-life is 2–5 minutes. The transcription rate  $k_{\text{tx}}$  spans  $2.5\text{--}50 \text{ min}^{-1}$ . The lower end represents standard constitutive promoters, while rates approaching  $50 \text{ min}^{-1}$  (nearly one initiation per second) correspond to highly active promoters such as those driving ribosomal RNA synthesis or fully induced viral genes. These rates produce mean burst sizes ranging from 0.5 to 10 transcripts per burst, consistent with experimental measures in prokaryotic systems. The resulting mean mRNA copy numbers at steady state range from approximately 0.3 to 5 transcripts per cell, typical of low-to-moderate expression bacterial genes where the majority of transcripts are present at fewer than 10 copies per cell. This bursty, low-copy number regime represents a challenging test case for inference due to the inherent sparsity and stochasticity of the data.

### Differentiable Histograms

**Triangular KDE.** To compare simulated and target distributions, we construct differentiable histograms using triangular kernel density estimation (KDE). For a batch of  $N_{\text{tot}}$  simulation outputs  $\{S_i\}_{i=1}^{N_{\text{tot}}}$  and  $B$  histogram bins with centers  $\{c_j\}_{j=1}^B$ , we first compute raw kernel affinities with bandwidth  $h$ :

$$k_{ij} = \max \left( 0, 1 - \frac{|S_i - c_j|}{h} \right)$$

Soft bin assignments are obtained by normalizing per sample,  $w_{ij} = k_{ij} / \sum_l k_{il}$ . This normalization ensures conservation of probability mass for samples near the grid boundaries, without biasing the estimation in the bulk. We employ a bandwidth equal to the bin width, corresponding to  $h = 1.0$  in the case of integer data in this work. This ensures that one grid point contributes exactly zero mass to neighboring bins, recovering the exact probability mass function. Crucially, this also maintains non-zero gradients for the bin assignments, yielding a differentiable estimator that avoids introducing smoothing artifacts for integer data, in contrast e.g. to the more common Gaussian kernel.

**Dirichlet smoothing.** The histogram count for bin  $j$  is  $h_j = \sum_{i=1}^{N_{\text{tot}}} w_{ij}$ . To ensure full support and numerical stability, we apply Dirichlet smoothing [43] with per-bin pseudocount  $\alpha$  and total number of bins  $B$ :

$$\hat{p}_j = \frac{h_j + \alpha}{\sum_{k=1}^B h_k + \alpha B}$$

This regularization prevents zero-probability singularities (e.g., in KL divergence) with minimal distortion to the distribution, avoiding the significant bias introduced by naive background mass addition.

**Variance reduction.** Accurately resolving the distribution, particularly in the tails, requires a large number of simulations, but backpropagating through all of them would exceed memory constraints. We therefore compute distributional statistics from a combined pool of  $N$  gradient-tracked simulations and  $M$  forward-only baseline simulations (detached from the computation graph), with  $N_{\text{tot}} = N + M$ . This decouples the sample size needed for accurate distribution estimates from the memory cost of gradient computation. As an additional benefit, this yields lower-variance gradient estimates at the cost of a controlled bias that is effectively absorbed by adaptive learning rate methods. A full account of the bias-variance trade-off is provided in Section S3.

### Optimization

The gradient estimates from the ST-GS estimator are used to optimize the simulation parameters via gradient-based methods. We employ the Adam optimizer [36], a modern adaptive variant of stochastic gradient descent

(SGD). Adam maintains exponential moving averages of gradients and their second moments to adapt learning rates on a per-parameter basis.

We found that the specific geometry of the loss landscapes in kinetic model inference requires careful optimizer tuning. These landscapes typically feature deep, narrow, and flat ridges (manifolds of sloppy parameters [35]) surrounded by steep walls. When initialization places parameters far from the optimum, initial gradients are extremely large, causing rapid accumulation of momentum and second-moment estimates in adaptive optimizers like Adam. This leads to two critical issues: (i) high accumulated momentum causes severe oscillations upon reaching the low-gradient valley, and (ii) the second-moment estimator “remembers” the large initial gradients, excessively dampening the effective learning rate once in the flat region where gradients are small. To mitigate these effects, we employ Adam with modified hyperparameters:  $\beta_1 = 0.8$  (reduced momentum) to minimize oscillations, and  $\beta_2 = 0.9$  (short-term memory for dampening) to allow the variance estimate to adapt

rapidly to the drastic change in gradient magnitude between the steep walls and the flat valley.

## ACKNOWLEDGMENTS

We thank Aidan Zentner and all members of the Brenner Group for valuable feedback and discussions. This work was supported by NSF AI Institute of Dynamic Systems 2112085, the Harvard MRSEC (NSF DMR-2011754) and the Office of Naval Research through grant number ONR N00014-23-1-2654.

## DATA AVAILABILITY

The Python library written to conduct this study is available at <https://github.com/fmottes/stochastix/>. Code and data for reproducing the experiments in this paper is available at <https://github.com/fmottes/stochastix-paper/>.

---

- [1] M. B. Elowitz, A. J. Levine, E. D. Siggia, and P. S. Swain, Stochastic gene expression in a single cell, *Science* **297**, 1183 (2002).
- [2] A. Raj and A. van Oudenaarden, Nature, nurture, or chance: Stochastic gene expression and its consequences, *Cell* **135**, 216 (2008).
- [3] A. Arkin, J. Ross, and H. H. McAdams, Stochastic kinetic analysis of developmental pathway bifurcation in phage  $\lambda$ -infected *Escherichia coli* cells, *Genetics* **149**, 1633 (1998).
- [4] E. M. Ozbudak, M. Thattai, H. N. Lim, B. I. Shraiman, and A. Van Oudenaarden, Multistability in the lactose utilization network of *Escherichia coli*, *Nature* **427**, 737 (2004).
- [5] U. Seifert, Stochastic thermodynamics, fluctuation theorems and molecular machines, *Reports on progress in physics* **75**, 126001 (2012).
- [6] C. Jarzynski, Nonequilibrium equality for free energy differences, *Physical Review Letters* **78**, 2690 (1997).
- [7] D. T. Gillespie, A rigorous derivation of the chemical master equation, *Physica A: Statistical Mechanics and its Applications* **188**, 404 (1992).
- [8] A. J. Black and A. J. McKane, Stochastic formulation of ecological models and their applications, *Trends in ecology & evolution* **27**, 337 (2012).
- [9] N. G. Van Kampen, *Stochastic processes in physics and chemistry*, Vol. 1 (Elsevier, 1992).
- [10] J. Schnakenberg, Network theory of microscopic and macroscopic behavior of master equation systems, *Reviews of Modern Physics* **48**, 571 (1976).
- [11] V. Shahrezaei and P. S. Swain, Analytical distributions for stochastic gene expression, *Proceedings of the National Academy of Sciences* **105**, 17256 (2008).
- [12] D. T. Gillespie, Exact stochastic simulation of coupled chemical reactions, *The Journal of Physical Chemistry* **81**, 2340 (1977).
- [13] B. Munsky and M. Khammash, The finite state projection algorithm for the solution of the chemical master equation, *The Journal of chemical physics* **124** (2006).
- [14] B. Munsky, G. Neuert, and A. Van Oudenaarden, Using gene expression noise to understand gene regulation, *Science* **336**, 183 (2012).
- [15] G. Neuert, B. Munsky, R. Z. Tan, L. Teytelman, M. Khammash, and A. Van Oudenaarden, Systematic identification of signal-activated stochastic gene regulation, *Science* **339**, 584 (2013).
- [16] Z. Fang, A. Gupta, S. Kumar, and M. Khammash, Advanced methods for gene network identification and noise decomposition from single-cell data, *Nature Communications* **15**, 4911 (2024).
- [17] C. Zechner, J. Ruess, P. Krenn, S. Pelet, M. Peter, J. Lygeros, and H. Koeppl, Moment-based inference predicts bimodality in transient gene expression, *Proceedings of the National Academy of Sciences* **109**, 8340 (2012).
- [18] T. Toni, D. Welch, N. Strelkowa, A. Ipsen, and M. P. Stumpf, Approximate bayesian computation scheme for parameter inference and model selection in dynamical systems, *Journal of the Royal Society Interface* **6**, 187 (2009).
- [19] J. Liepe, P. Kirk, S. Filippi, T. Toni, C. P. Barnes, and M. P. Stumpf, A framework for parameter estimation and model selection from experimental data in systems biology using approximate bayesian computation, *Nature protocols* **9**, 439 (2014).
- [20] A. Golightly and D. J. Wilkinson, Bayesian parameter inference for stochastic biochemical network models using particle markov chain monte carlo, *Interface focus* **1**, 807 (2011).
- [21] C. Andrieu, A. Doucet, and R. Holenstein, Particle markov chain monte carlo methods, *Journal of the Royal Statistical Society Series B: Statistical Methodology* **72**,

269 (2010).

[22] A. G. Baydin, B. A. Pearlmutter, A. A. Radul, and J. M. Siskind, Automatic differentiation in machine learning: a survey, *Journal of machine learning research* **18**, 1 (2018).

[23] S. Plyasunov and A. P. Arkin, Efficient stochastic sensitivity analysis of discrete event systems, *Journal of Computational Physics* **221**, 724 (2007).

[24] A. Gupta and M. Khammash, Unbiased estimation of parameter sensitivities for stochastic chemical reaction networks, *SIAM Journal on Scientific Computing* **35**, A2598 (2013).

[25] D. F. Anderson, An efficient finite difference method for parameter sensitivities of continuous time markov chains, *SIAM Journal on Numerical Analysis* **50**, 2237 (2012).

[26] K. Rijal and P. Mehta, A differentiable gillespie algorithm for simulating chemical kinetics, parameter estimation, and designing synthetic biological circuits, *eLife* **14**, RP103877 (2025).

[27] E. Jang, S. Gu, and B. Poole, Categorical reparameterization with gumbel-softmax, *arXiv preprint arXiv:1611.01144* (2017), arXiv:arXiv:1611.01144 [stat.ML].

[28] C. J. Maddison, A. Mnih, and Y. W. Teh, The concrete distribution: A continuous relaxation of discrete random variables, *arXiv preprint arXiv:1611.00712* (2017), arXiv:arXiv:1611.00712 [stat.ML].

[29] J. Peccoud and B. Ycart, Markovian modeling of gene-product synthesis, *Theoretical population biology* **48**, 222 (1995).

[30] I. Golding, J. Paulsson, S. M. Zawilski, and E. C. Cox, Real-time kinetics of gene activity in individual bacteria, *Cell* **123**, 1025 (2005).

[31] L.-h. So, A. Ghosh, C. Zong, L. A. Sepúlveda, R. Segev, and I. Golding, General properties of transcriptional time series in escherichia coli, *Nature genetics* **43**, 554 (2011).

[32] A. Raj, C. S. Peskin, D. Tranchina, D. Y. Vargas, and S. Tyagi, Stochastic mrna synthesis in mammalian cells, *PLoS biology* **4**, e309 (2006).

[33] D. M. Suter, N. Molina, D. Gatfield, K. Schneider, U. Schibler, and F. Naeff, Mammalian genes are transcribed with widely different bursting kinetics, *science* **332**, 472 (2011).

[34] G. Gorin, J. J. Vastola, M. Fang, and L. Pachter, Interpretable and tractable models of transcriptional noise for the rational design of single-molecule quantification experiments, *Nature Communications* **13**, 7620 (2022).

[35] R. N. Gutenkunst, J. J. Waterfall, F. P. Casey, K. S. Brown, C. R. Myers, and J. P. Sethna, Universally sloppy parameter sensitivities in systems biology models, *PLoS computational biology* **3**, e189 (2007).

[36] D. P. Kingma and J. Ba, Adam: A method for stochastic optimization, *arXiv preprint arXiv:1412.6980* (2014), arXiv:arXiv:1412.6980 [cs.LG].

[37] G. Peyré, M. Cuturi, *et al.*, Computational optimal transport: With applications to data science, *Foundations and Trends® in Machine Learning* **11**, 355 (2019).

[38] T. L. Hill, *Free Energy Transduction and Biochemical Cycle Kinetics* (Springer-Verlag, 1989).

[39] C. Maes, Frenesy: Time-symmetric dynamical activity in nonequilibria, *Physics Reports* **850**, 1 (2020).

[40] L. Onsager, Reciprocal relations in irreversible processes. i., *Physical review* **37**, 405 (1931).

[41] J. Bradbury, R. Frostig, P. Hawkins, M. J. Johnson, C. Leary, D. Maclaurin, G. Necula, A. Paszke, J. Vander-Plas, S. Wanderman-Milne, and Q. Zhang, Jax: Composable transformations of python+numpy programs (2018), version 0.3.13.

[42] P. Kidger, C. Garcia, F. Bonnet, H. Oberhauser, J. Morrill, J. James, and T. Lyons, Equinox: Neural networks in jax via callable pytrees and filtered transformations, *arXiv preprint arXiv:2111.00254* (2021), arXiv:arXiv:2111.00254 [cs.LG].

[43] C. M. Bishop, *Pattern Recognition and Machine Learning* (Springer, 2006).

## SUPPLEMENTARY INFORMATION

### Gradient-based optimization of exact stochastic kinetic models

Francesco Mottes, Qian-Ze Zhu, and Michael P. Brenner

*School of Engineering and Applied Sciences, Harvard University, Cambridge MA 02138*

#### S1. DETAILS OF STRAIGHT-THROUGH GUMBEL-SOFTMAX GRADIENT ESTIMATION

Stochastic trajectories are generated using the Gillespie Direct Method [12], an exact algorithm for sampling from the probability distribution defined by the Chemical Master Equation. For a system in state  $\mathbf{x}$  at time  $t$ , the probability density of reaction  $j$  occurring at time  $t + \tau$  is

$$p(j, \tau \mid \mathbf{x}, t) = a_j(\mathbf{x}; \theta) \exp(-a_0(\mathbf{x}; \theta)\tau),$$

where  $a_j(\mathbf{x}; \theta)$  is the propensity of reaction  $j$  in state  $\mathbf{x}$  with parameter set  $\theta$ , and  $a_0(\mathbf{x}; \theta) = \sum_j a_j(\mathbf{x}; \theta)$  is the total propensity. The Direct Method involves two sampling operations at each step. First, the waiting time  $\Delta t$  is drawn from an exponential distribution with rate  $a_0$  via inverse transform sampling,

$$\Delta t = -\frac{\ln u}{a_0},$$

with  $u \sim \mathcal{U}(0, 1)$ . Second, the reaction index  $r$  is drawn from a categorical distribution with probabilities  $\pi_k = a_k/a_0$ . The system state is then updated according to the selected reaction,

$$\mathbf{x}(t + \Delta t) = \mathbf{x}(t) + \mathbf{S}_{:,r},$$

where  $\mathbf{S}_{:,r}$  denotes the  $r$ -th column of the stoichiometry matrix  $\mathbf{S}$ , representing the net change in species counts due to reaction  $r$ .

The waiting time  $\Delta t$  is already expressed as a differentiable function of the parameters through  $a_0(\theta)$ , with the stochastic component  $u$  held fixed. The categorical sampling of reaction identity requires additional treatment. The Gumbel-Max trick expresses the discrete sample as a deterministic function of parameter-independent random draws. If  $u_k \sim \mathcal{U}(0, 1)$  are independent samples and  $g_k = -\log(-\log u_k)$  are the corresponding standard Gumbel variates, then

$$y = \text{one\_hot} \left( \arg \max_k (g_k + \log \pi_k) \right)$$

samples from the categorical distribution with probabilities  $\pi_k = a_k/a_0$ . The one-hot vector  $y$  satisfies  $y_j = \delta_{j,r}$ , where  $\delta_{j,r}$  is the Kronecker delta and  $r$  is the selected reaction index. The state update can then be written as

$$\mathbf{x}(t + \Delta t) = \mathbf{x}(t) + \mathbf{S}y,$$

expressing the update as a matrix-vector product rather than an indexing operation.

The  $\arg \max$  operation has zero gradients almost everywhere. The Straight-Through Gumbel-Softmax (ST-GS) estimator approximates gradients using the continuous Gumbel-Softmax relaxation,

$$\tilde{y}_k = \frac{\exp((g_k + \log \pi_k)/\tau)}{\sum_j \exp((g_j + \log \pi_j)/\tau)},$$

where the temperature parameter  $\tau > 0$  controls the smoothness of the approximation. As  $\tau \rightarrow 0$ , the softmax output concentrates toward the  $\arg \max$ . The straight-through estimator uses the discrete

sample  $y$  in the forward pass while backpropagating gradients through the continuous approximation  $\tilde{y}$ . This is implemented as

$$y_{\text{ST}} = \tilde{y} + \text{stop\_gradient}(y - \tilde{y}),$$

where  $\text{stop\_gradient}(\cdot)$  denotes an operation that evaluates to its argument in the forward pass but has zero gradient in the backward pass. In the forward pass,  $y_{\text{ST}} = y$  since the stop-gradient term evaluates to  $y - \tilde{y}$ . In the backward pass, the gradient flows only through  $\tilde{y}$ .

Using the normalized probabilities  $\pi_k = a_k/a_0$  rather than raw propensities  $a_k$  in the softmax relaxation ensures that gradients correctly capture the constraint  $\sum_k \pi_k = 1$ . Specifically, increasing one propensity  $a_j$  affects all probabilities through the normalization,

$$\frac{\partial \pi_k}{\partial a_j} = \frac{\delta_{k,j}}{a_0} - \frac{a_k}{a_0^2} = \frac{1}{a_0} (\delta_{k,j} - \pi_k),$$

and this coupling is correctly propagated when gradients are computed through  $\log \pi_k$ .

## S2. DERIVATION OF THE PARETO-OPTIMAL CURRENT BOUND

We derive here the theoretical upper bound on the steady-state current  $J$  achievable in a three-state unicyclic network, subject to a fixed thermodynamic affinity  $\mathcal{A}$  and a fixed total kinetic budget  $K_{\text{tot}}$ .

Consider a ring of  $N = 3$  states with periodic boundary conditions, where transitions from state  $i$  to state  $i + 1$  (mod 3) occur with forward rate  $k_i^+$  and backward rate  $k_i^-$ . The system is subject to two constraints. The first is a kinetic budget constraint on the total rate constant expenditure,

$$K_{\text{tot}} = \sum_{i=1}^3 (k_i^+ + k_i^-).$$

The second is a thermodynamic constraint fixing the cycle affinity,

$$\mathcal{A} = \ln \prod_{i=1}^3 \frac{k_i^+}{k_i^-} = \sum_{i=1}^3 \ln \frac{k_i^+}{k_i^-}.$$

The affinity quantifies the thermodynamic driving force around the cycle and is related to the entropy production rate by  $\sigma = J\mathcal{A}$ .

In a three-state ring, current must pass through all three edges to complete a cycle. If rates are distributed unevenly, the edge with the smallest net forward bias acts as a bottleneck limiting the overall flux. Redistributing rates to equalize the edges removes this bottleneck without changing the total affinity. The optimal configuration is therefore symmetric:

$$k_1^+ = k_2^+ = k_3^+ \equiv k_+, \quad k_1^- = k_2^- = k_3^- \equiv k_-.$$

In this symmetric regime, the constraints reduce to

$$K_{\text{tot}} = 3(k_+ + k_-), \quad \mathcal{A} = 3 \ln \frac{k_+}{k_-},$$

which can be inverted to yield

$$k_+ + k_- = \frac{K_{\text{tot}}}{3}, \quad \frac{k_+}{k_-} = e^{\mathcal{A}/3}.$$

By symmetry, the steady-state occupation probabilities are uniform,  $\pi_i = 1/3$  for all  $i$ . The net current across any edge is therefore

$$J = \pi_i k_+ - \pi_{i+1} k_- = \frac{1}{3}(k_+ - k_-).$$

To express  $J$  solely in terms of the constraint parameters, we rewrite the difference of rates as

$$J = \frac{1}{3}(k_+ - k_-) = \frac{K_{\text{tot}}}{9} \cdot \frac{k_+ - k_-}{k_+ + k_-},$$

where we have substituted the budget constraint in the equality. Dividing numerator and denominator by  $k_-$  and introducing  $\rho = k_+/k_- = e^{\mathcal{A}/3}$  gives

$$J = \frac{K_{\text{tot}}}{9} \cdot \frac{\rho - 1}{\rho + 1} = \frac{K_{\text{tot}}}{9} \cdot \frac{e^{\mathcal{A}/3} - 1}{e^{\mathcal{A}/3} + 1}.$$

Using the identity  $(e^{2x} - 1)/(e^{2x} + 1) = \tanh(x)$  with  $x = \mathcal{A}/6$ , we obtain the Pareto-optimal bound,

$$J^*(\mathcal{A}, K_{\text{tot}}) = \frac{K_{\text{tot}}}{9} \tanh\left(\frac{\mathcal{A}}{6}\right).$$

This bound interpolates between two physical regimes. In the linear response regime where  $\mathcal{A} \ll 1$ , expanding  $\tanh(x) \approx x$  gives the Onsager-like linear flux-force relation,

$$J^* \approx \frac{K_{\text{tot}}}{54} \mathcal{A}.$$

Using  $\mathcal{A} = \sigma/J$  to eliminate the affinity in favor of entropy production, we obtain the square-root scaling of current with dissipation near equilibrium  $J^* \propto \sqrt{\sigma}$ .

In the far-from-equilibrium limit  $\mathcal{A} \rightarrow \infty$ , the hyperbolic tangent saturates to unity and the current approaches a kinetically limited maximum,

$$J_{\text{max}}^* = \frac{K_{\text{tot}}}{9},$$

independent of the driving force.

### S3. VARIANCE-REDUCED GRADIENT ESTIMATION WITH BASELINE SIMULATIONS

We optimize model parameters  $\theta$  by minimizing a loss function  $L(\theta)$  that quantifies the discrepancy between target statistics and distributions generated by stochastic simulations  $S(\theta)$ . The loss involves expectations over simulation outputs,  $L(\theta) = f(\mathbb{E}[g_1(S)], \mathbb{E}[g_2(S)], \dots)$ , which we estimate via Monte Carlo sampling to yield  $L_{MC}(\theta)$ . Standard gradient descent on  $\nabla_\theta L_{MC}(\theta)$  often exhibits high variance, impeding stable convergence.

We implement a variance reduction technique that introduces a controlled bias in exchange for substantially lower gradient variance. At each optimization step, we generate two distinct simulation sets:  $N$  gradient-tracked simulations  $\{S_i(\theta)\}_{i=1}^N$  with retained computation graphs, and  $M$  baseline simulations  $\{B_j(\theta)\}_{j=1}^M$  detached from the gradient computation (e.g., via `jax.lax.stop_gradient` in JAX).

We compute all empirical estimators using the combined pool of  $N + M$  simulations. For a function  $g(S)$ , the estimator is:

$$\hat{\mathbb{E}}[g(S)] = \frac{1}{N + M} \left( \sum_{i=1}^N g(S_i(\theta)) + \sum_{j=1}^M g(B_j(\theta)) \right)$$

This yields low-variance estimates for the summary statistics, with Monte Carlo error scaling as  $(N + M)^{-1/2}$ . When computing  $\nabla_\theta L_{MC}(\theta)$ , the baseline simulations act as constants:

$$\nabla_\theta \hat{\mathbb{E}}[g(S)] = \frac{1}{N + M} \sum_{i=1}^N \nabla_\theta g(S_i(\theta))$$

This approach decouples the precision of the loss evaluation (using  $N + M$  samples) from the cost of gradient computation (using  $N$  samples).

**Bias characterization.** The resulting gradient estimator is biased. To derive the bias, we first note that the reparameterization underlying the ST-GS estimator allows interchange of differentiation and expectation (the pathwise gradient identity):

$$\nabla_{\theta} \mathbb{E}[g(S)] = \mathbb{E}[\nabla_{\theta} g(S)].$$

The standard Monte Carlo estimator using  $N$  samples yields an unbiased estimate:

$$\frac{1}{N} \sum_{i=1}^N \nabla_{\theta} g(S_i) \Rightarrow \mathbb{E} \left[ \frac{1}{N} \sum_{i=1}^N \nabla_{\theta} g(S_i) \right] = \mathbb{E}[\nabla_{\theta} g(S)] = \nabla_{\theta} \mathbb{E}[g(S)].$$

In contrast, our estimator uses only  $N$  gradient-tracked samples but normalizes by  $N + M$ . Denoting this estimator by  $\hat{\Sigma}_{\text{biased}}$ :

$$\hat{\Sigma}_{\text{biased}} = \frac{1}{N + M} \sum_{i=1}^N \nabla_{\theta} g(S_i).$$

Taking expectations over the simulation randomness gives

$$\mathbb{E} \left[ \hat{\Sigma}_{\text{biased}} \right] = \frac{N}{N + M} \mathbb{E}[\nabla_{\theta} g(S)] = \frac{N}{N + M} \nabla_{\theta} \mathbb{E}[g(S)].$$

Thus the estimator is shrunk by a factor  $N/(N + M)$ .

This characterization holds exactly for estimating sensitivities of the form  $\nabla_{\theta} \mathbb{E}[g(S)]$ . In the full loss  $L = f(\mathbb{E}[g(S)])$ , additional bias can arise from the nonlinearity of  $f$ . However, in the large- $M$  limit, the forward estimate of  $\mathbb{E}[g(S)]$  becomes effectively deterministic, and the multiplicative shrinkage derived above becomes the dominant source of bias.

**Variance reduction.** To analyze the variance reduction, we decompose the gradient using the chain rule. For simplicity, consider a loss depending on a single expectation,  $L = f(\mathbb{E}[g(S)])$ . The gradient is:

$$\nabla_{\theta} L = \underbrace{\frac{\partial f}{\partial \mathbb{E}[g(S)]}}_{\text{Error Signal } E} \cdot \underbrace{\nabla_{\theta} \mathbb{E}[g(S)]}_{\text{Sensitivity } \Sigma}$$

Both terms benefit from using the larger sample pool: the first through reduced error signal variance  $\mathcal{O}(1/(N + M))$ , the second through reduced sensitivity variance  $\mathcal{O}(N/(N + M)^2)$ .

a. *Error signal variance.* The error signal  $E$  depends on the estimated expectation  $\hat{\mathbb{E}}[g(S)]$ . Using all  $N + M$  samples:

$$\text{Var}(\hat{\mathbb{E}}[g(S)]) = \frac{\text{Var}(g(S))}{N + M}$$

By the delta method, the variance of  $E = f'(\hat{\mathbb{E}}[g(S)])$  scales as:

$$\text{Var}(E) \approx (f''(\mathbb{E}[g(S)]))^2 \frac{\text{Var}(g(S))}{N + M} = \mathcal{O} \left( \frac{1}{N + M} \right)$$

compared to  $\mathcal{O}(1/N)$  when using only the  $N$  gradient-tracked samples.

b. *Sensitivity variance.* For the unbiased (bias-corrected) estimator, the sensitivity estimate is:

$$\hat{\Sigma}_{\text{unbiased}} = \frac{1}{N} \sum_{i=1}^N \nabla_{\theta} g(S_i(\theta))$$

with variance  $\text{Var}(\hat{\Sigma}_{\text{unbiased}}) = \text{Var}(\nabla_{\theta} g(S))/N = \mathcal{O}(1/N)$ .

For the biased estimator:

$$\hat{\Sigma}_{\text{biased}} = \frac{1}{N+M} \sum_{i=1}^N \nabla_{\theta} g(S_i(\theta))$$

The variance is:

$$\text{Var}(\hat{\Sigma}_{\text{biased}}) = \frac{1}{(N+M)^2} \cdot N \cdot \text{Var}(\nabla_{\theta} g(S)) = \frac{N}{(N+M)^2} \text{Var}(\nabla_{\theta} g(S)) = \mathcal{O}\left(\frac{N}{(N+M)^2}\right)$$

Note that if we rescale  $\hat{\Sigma}_{\text{biased}}$  by  $(N+M)/N$  to remove the shrinkage bias, its variance returns to  $\mathcal{O}(1/N)$ ; thus the primary variance reduction comes from stabilizing the error signal  $E$  via the larger  $N+M$  sample pool.

**Practical considerations.** During optimization, the multiplicative shrinkage factor  $N/(N+M)$  in the sensitivity estimate is effectively absorbed by adaptive optimizers such as Adam: if the gradient is scaled by an approximately constant factor, Adam's moment normalization renders the update nearly scale-invariant. Empirically, we find that optimization proceeds well without explicit corrections.

While this technique can stabilize the estimation of all summary statistics, it is particularly useful for differentiable histogram-based objectives, which require large sample sizes to accurately populate bins. Memory constraints often limit the number of concurrent gradient-tracked simulations, but forward-only simulations are much cheaper in both memory and computation time. By augmenting a small set of gradient-tracked trajectories with a large pool of forward-only simulations, we can greatly reduce Monte Carlo noise in the histogram—and hence in the error signal  $E$ —without exceeding hardware limits.

## MOMENT MATCHING

**Experiment Details.** We inferred two parameters of the telegraph promoter model ( $k_{\text{on}}$  and  $k_{\text{tx}}$ ) from the mean and variance of steady-state RNA copy numbers, with  $k_{\text{off}}$  and  $k_{\text{mdeg}}$  fixed to their ground-truth values. Each optimization used 512 gradient-tracked simulations combined with 1000 baseline (forward-only) simulations per epoch for variance reduction. Parameters were initialized randomly within  $[0.2 \times, 5 \times]$  the true values. Rate constants were parameterized as  $k = e^\phi$  and optimization was performed over the log-transformed variables  $\phi$ . Training ran for 100 epochs using Adam with learning rate lr = 0.1 and modified hyperparameters ( $\beta_1 = 0.8$ ,  $\beta_2 = 0.9$ ).

**Additional Results.** Fig. S1 shows loss trajectories and parameter recovery for all 25 parameter sets. Both  $k_{\text{on}}$  and  $k_{\text{tx}}$  are recovered accurately, with optimized values clustering near the true parameters regardless of trajectory duration.

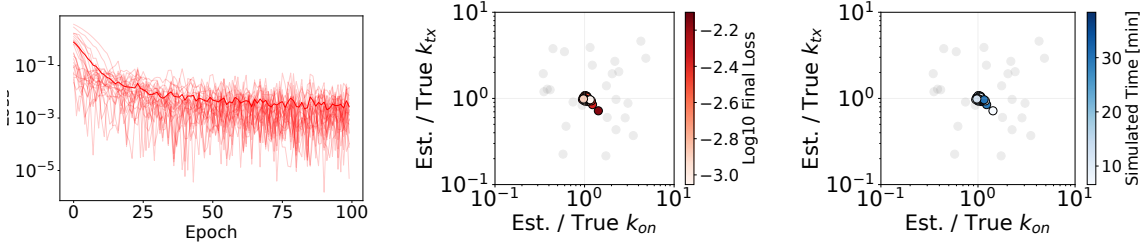


**FIG. S1. Moment matching optimization results.** **(Left)** Loss trajectories for all 25 parameter sets of the telegraph promoter model. Light curves show individual runs; dark curve shows the mean. **(Center)** Parameter recovery accuracy: ratio of estimated to true parameter values for  $k_{\text{on}}$  and  $k_{\text{tx}}$ . Gray points show initial guesses; colored points show optimized values, with color indicating final loss. Optimized parameters cluster near the true values (intersection of gray lines at ratio 1). **(Right)** Same data as center panel, with color indicating the simulated trajectory duration.

## DISTRIBUTION MATCHING

**Experiment Details.** We inferred three parameters of the telegraph promoter model ( $k_{\text{on}}$ ,  $k_{\text{tx}}$ ,  $k_{\text{mdeg}}$ ) from steady-state RNA copy number distributions, with  $k_{\text{off}}$  fixed to its ground-truth value. Target distributions were generated by simulating 5000 trajectories to steady state for each of the 25 parameter sets. We minimized the 1-Wasserstein distance between target and simulated distribution functions. Differentiable histograms were constructed using triangular kernel density estimation with unit bandwidth and Dirichlet smoothing ( $\alpha = 0.1$ ). Each optimization used 512 gradient-tracked simulations combined with 4488 baseline (forward-only) simulations per epoch. Parameters were initialized randomly within  $[0.2 \times, 5 \times]$  the true values. Rate constants were parameterized as  $k = e^\phi$  and optimization was performed over the log-transformed variables  $\phi$ . Training ran for 100 epochs using Adam with learning rate  $\text{lr} = 0.1$  and modified hyperparameters ( $\beta_1 = 0.8$ ,  $\beta_2 = 0.9$ ).

**Additional Results.** Figs. S2–S6 show optimization results. The transcription rate  $k_{\text{tx}}$  is recovered most accurately ( $r = 0.974$ ), while  $k_{\text{on}}$  and  $k_{\text{mdeg}}$  show moderate correlations ( $r = 0.747$  and  $r = 0.800$ ). The correlated scatter in the  $k_{\text{on}}\text{--}k_{\text{mdeg}}$  plane reflects the known degeneracy where these parameters jointly control burst frequency.

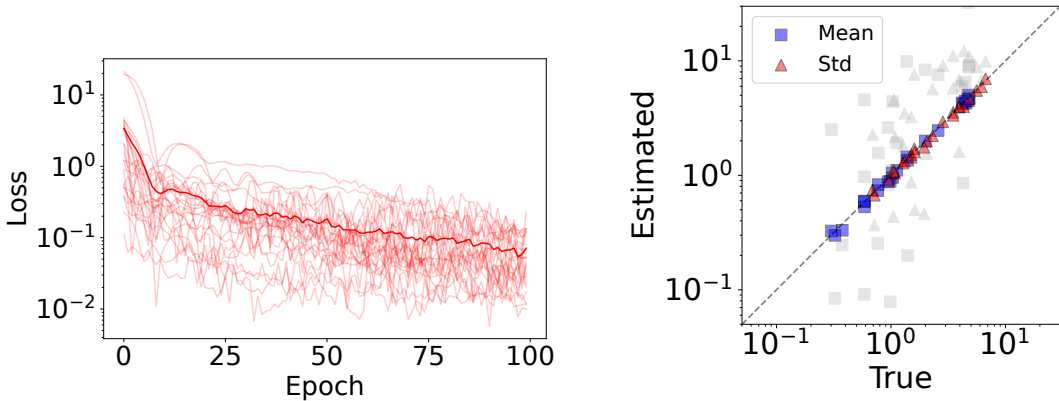


**FIG. S2. Distribution matching optimization summary.** **(Left)** Loss trajectories for all 25 parameter sets. Light curves show individual runs; dark curve shows the mean. **(Right)** Recovery of target distribution statistics. Estimated vs. true mean (blue squares) and standard deviation (red triangles) of the RNA copy number distribution. Gray markers show initial guesses; colored markers show optimized values.

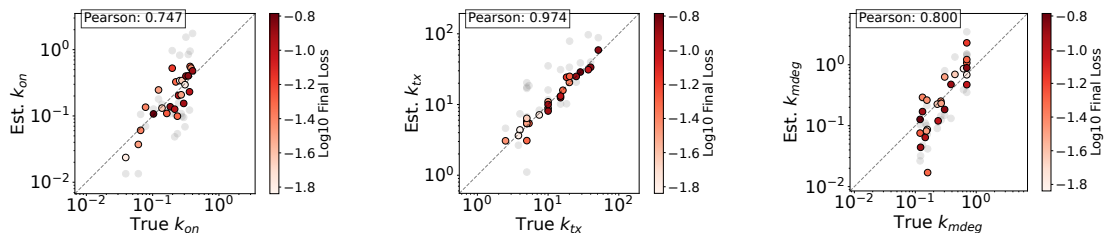


**FIG. S3. Individual parameter recovery for distribution matching.** Estimated vs. true values for **(Left)**  $k_{\text{on}}$ , **(Center)**  $k_{\text{tx}}$ , and **(Right)**  $k_{\text{mdeg}}$ . Gray points show initial guesses; colored points show optimized values, with color indicating final loss. Pearson correlation coefficients are shown for each parameter. The transcription rate  $k_{\text{tx}}$  is recovered most accurately ( $r = 0.974$ ), while  $k_{\text{on}}$  and  $k_{\text{mdeg}}$  show moderate correlations ( $r = 0.747$  and  $r = 0.800$ , respectively).

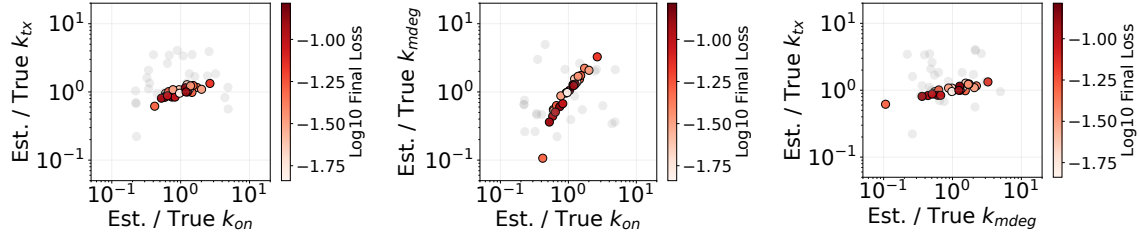


FIG. S4. **Pairwise parameter recovery for distribution matching.** Ratio of estimated to true parameter values shown in two-dimensional projections: (Left)  $k_{on}$  vs.  $k_{tx}$ , (Center)  $k_{on}$  vs.  $k_{mdeg}$ , and (Right)  $k_{mdeg}$  vs.  $k_{tx}$ . Gray points show initial guesses; colored points show optimized values, with color indicating final loss.

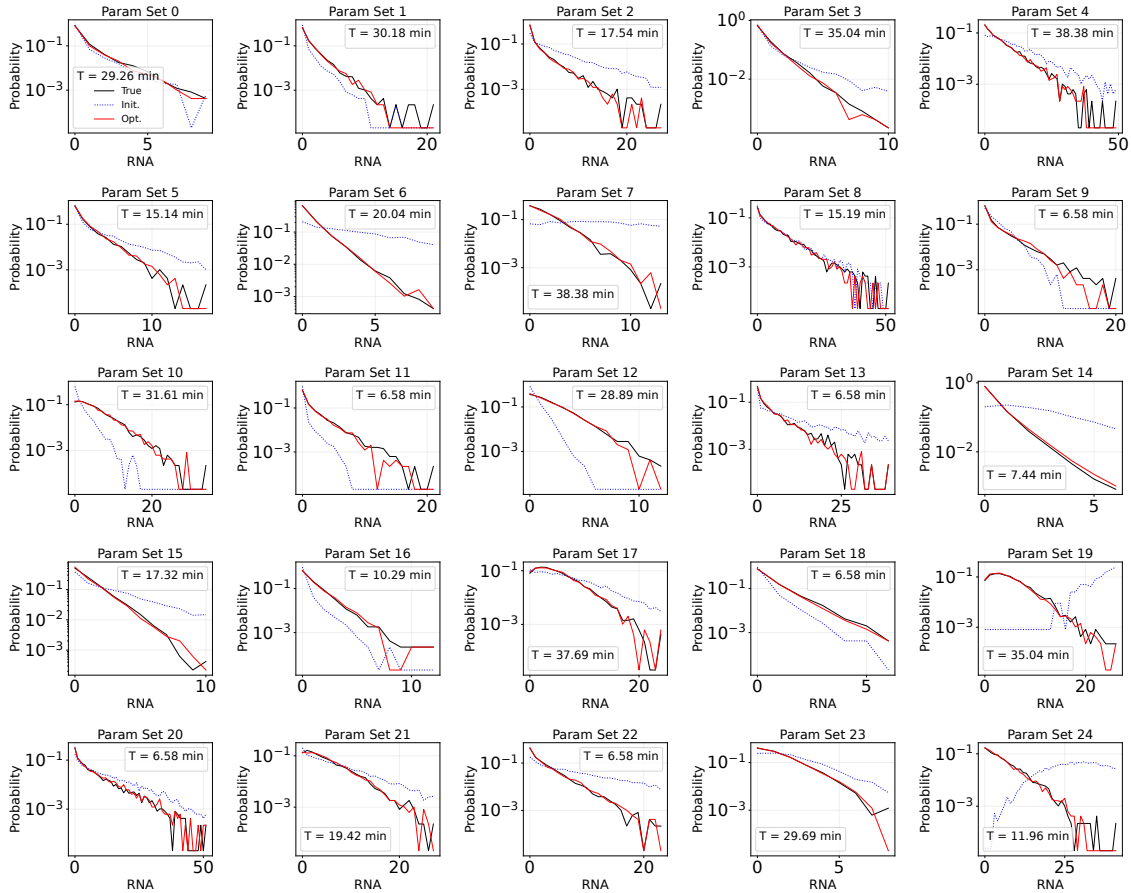


FIG. S5. **Distribution matching results across 25 parameter sets (log scale).** Comparison of steady-state RNA copy number distributions for the telegraph promoter model. Black: true distribution; blue dotted: initial guess; red: optimized parameters. The  $y$ -axis shows probability on a logarithmic scale, highlighting the fit quality in the distribution tails. Optimization time  $T$  is indicated for each parameter set.

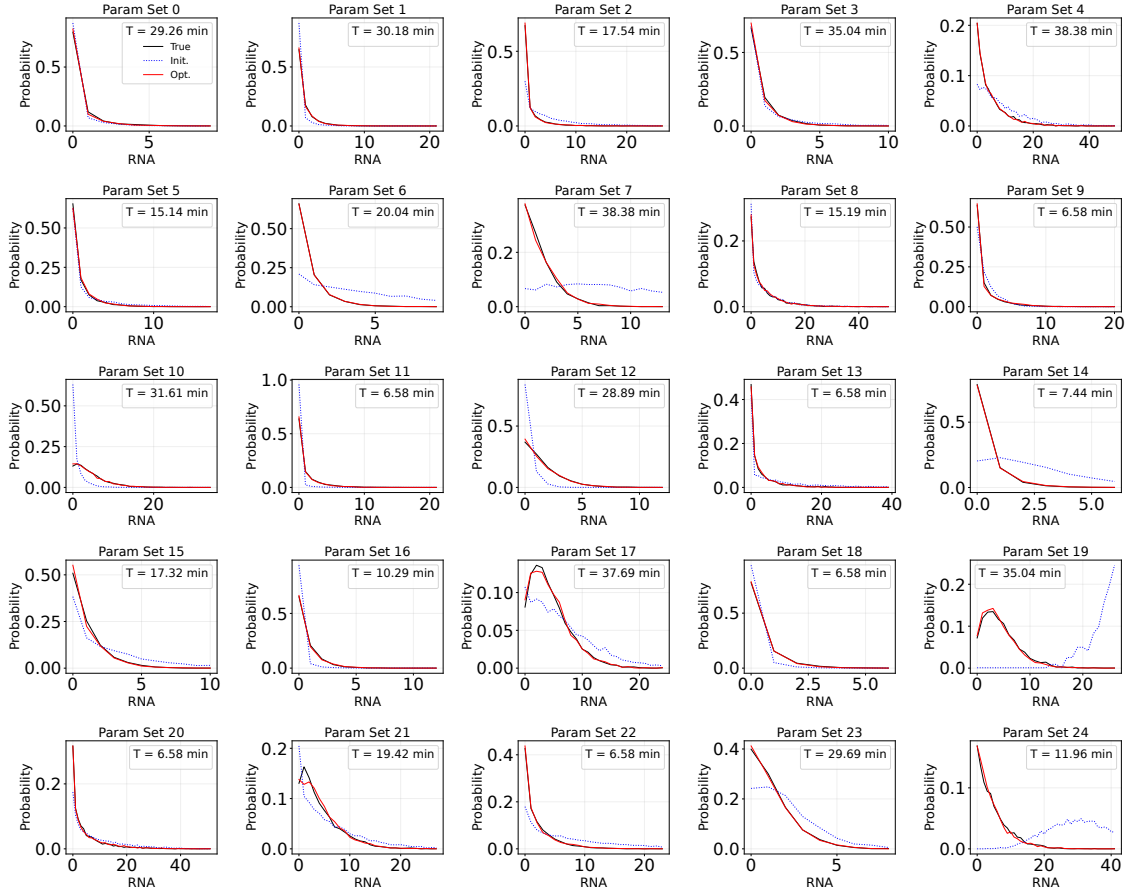


FIG. S6. Distribution matching results across 25 parameter sets (linear scale). Same data as Fig. S5 plotted with linear probability axes.

### THREE-STATE NON-EQUILIBRIUM CYCLE MODEL

**Experiment Details.** We optimized the cycle current  $J$  subject to constraints on entropy production rate  $\sigma$  and total kinetic budget  $K_{\text{tot}} = 1$ . Target entropy production values were logarithmically spaced between  $\sigma_{\text{min}} = 0.01$  and  $\sigma_{\text{max}} = 2.5$ , yielding 10 optimization targets. Constraints were enforced via penalty terms with coefficients  $\lambda_\sigma = \lambda_{K_{\text{tot}}} = 100$ . Rate constants were parameterized as  $k = e^\phi$  and optimization was performed over the log-transformed variables  $\phi$ . Training ran for 1000 epochs using Adam with learning rate lr = 0.05 and modified hyperparameters ( $\beta_1 = 0.8$ ,  $\beta_2 = 0.9$ ). Gradient estimates were computed from batches of 32 independent trajectories, each simulated for  $T_{\text{sim}} = 500$  time units.

**Additional Results.** Table S1 reports the optimized current  $J$ , achieved entropy production  $\sigma$ , and total kinetic budget  $K_{\text{tot}}$  for each target, along with relative errors compared to theoretical predictions. The kinetic budget constraint is satisfied to within 0.24% across all runs. Relative errors in current range from  $-6.9\%$  to  $+2.9\%$ , with larger deviations at low  $\sigma$  where the absolute current is small. Table S2 reports the optimized rate constants. At high dissipation ( $\sigma \gtrsim 1$ ), the forward rates converge to the symmetric allocation  $k_{ij}^+ \approx K_{\text{tot}}/9 \approx 0.333$ . At low dissipation, individual forward rates show substantial heterogeneity while their mean remains close to theory. Fig. S7 shows the Pareto front, Fig. S8 the optimized rates, and Fig. S9 the absolute and relative errors. Figs. S10–S19 show detailed optimization trajectories for each target  $\sigma$ .

$\sigma_{\text{target}}$	$\sigma$	$\Delta\sigma (\%)$	$J$	$J^*$	$\Delta J (\%)$	$K_{\text{tot}}$	$\Delta K_{\text{tot}} (\%)$
0.010	0.0105	+5.12	0.0143	0.0139	+2.85	0.9998	-0.02
0.018	0.0199	+7.54	0.0193	0.0191	+1.20	1.0011	+0.11
0.034	0.0339	-0.47	0.0231	0.0249	-6.90	0.9996	-0.04
0.063	0.0619	-1.81	0.0310	0.0333	-6.90	0.9993	-0.07
0.116	0.1142	-1.84	0.0434	0.0447	-2.86	0.9982	-0.18
0.215	0.2161	+0.55	0.0593	0.0598	-0.82	1.0006	+0.06
0.397	0.3991	+0.56	0.0767	0.0774	-0.89	1.0024	+0.24
0.733	0.7339	+0.13	0.0959	0.0953	+0.63	1.0022	+0.22
1.354	1.3540	+0.03	0.1099	0.1078	+1.98	0.9992	-0.08
2.500	2.5020	+0.08	0.1128	0.1110	+1.66	1.0001	+0.01

TABLE S1. **Pareto front optimization results.** For each target entropy production  $\sigma_{\text{target}}$ : achieved entropy production  $\sigma$ , optimized current  $J$ , theoretical current  $J^*$ , achieved kinetic budget  $K_{\text{tot}}$ , and relative errors. Theory assumes optimal symmetric allocation.

$\sigma_{\text{target}}$	$k_{12}^+$	$k_{23}^+$	$k_{31}^+$	$k^-$	$k_{\text{theory}}^+$	$k_{\text{theory}}^-$
0.010	0.232	0.249	0.098	0.140	0.188	0.146
0.018	0.245	0.255	0.104	0.132	0.195	0.138
0.034	0.255	0.261	0.114	0.123	0.204	0.129
0.063	0.277	0.268	0.128	0.109	0.217	0.117
0.116	0.297	0.278	0.147	0.093	0.234	0.100
0.215	0.329	0.277	0.175	0.073	0.256	0.077
0.397	0.373	0.279	0.210	0.047	0.283	0.051
0.733	0.392	0.287	0.259	0.022	0.310	0.024
1.354	0.335	0.327	0.324	0.005	0.328	0.005
2.500	0.333	0.333	0.333	0.0002	0.333	0.0002

TABLE S2. **Optimized rate constants.** Forward rates  $k_{12}^+$ ,  $k_{23}^+$ ,  $k_{31}^+$  and common backward rate  $k^-$  for each target entropy production. Theory columns show predictions for optimal symmetric allocation.

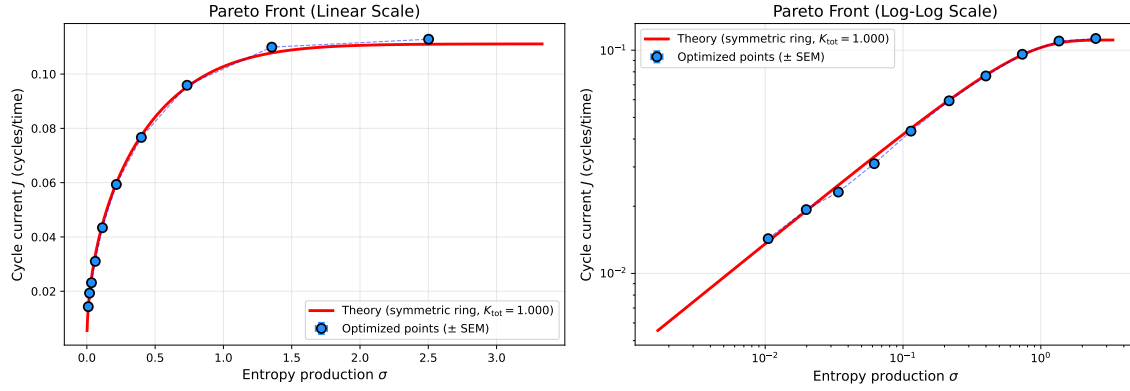


FIG. S7. **Pareto front for the three-state cycle model.** Optimized steady-state current  $J$  as a function of entropy production rate  $\sigma$  for fixed kinetic budget  $K_{\text{tot}} = 1$ . **(Left)** Linear scale. **(Right)** Log-log scale. Red curve: theoretical Pareto-optimal bound derived for symmetric rate allocation (Section S2). Blue points: optimized values.

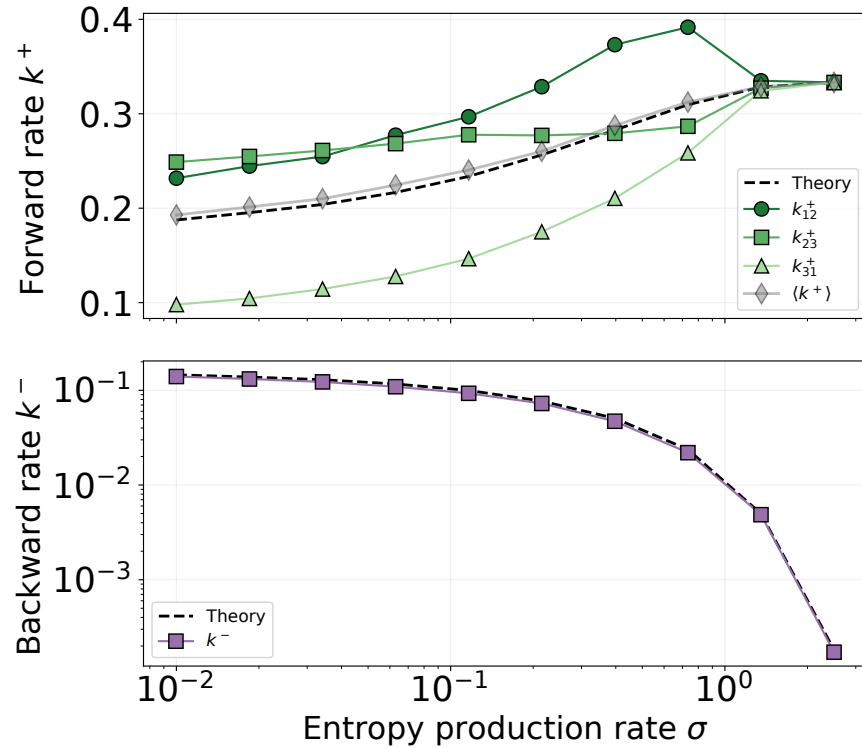


FIG. S8. **Optimized rate constants along the Pareto front.** **(Top)** Forward rates  $k_{ij}^+$  for each edge of the three-state cycle. Individual rates (colored markers) show some heterogeneity, but the mean  $\langle k^+ \rangle$  (gray diamonds) closely tracks the theoretical prediction for symmetric allocation (dashed line). **(Bottom)** Backward rates  $k^-$  (purple squares) compared to theory.

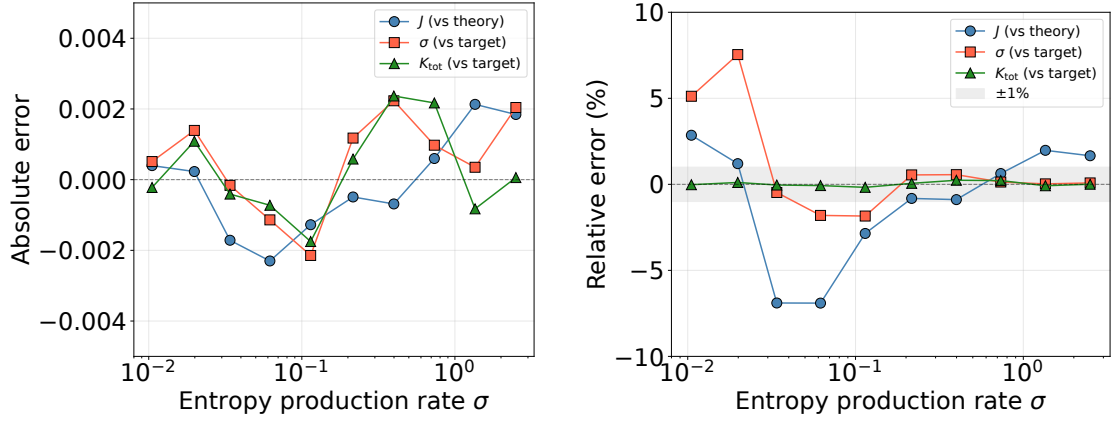


FIG. S9. **Optimization accuracy for the three-state cycle.** (Left) Absolute errors and (Right) relative errors for the optimized current  $J$  (vs. theoretical bound), entropy production  $\sigma$  (vs. target), and kinetic budget  $K_{\text{tot}}$  (vs. target) as a function of entropy production rate.

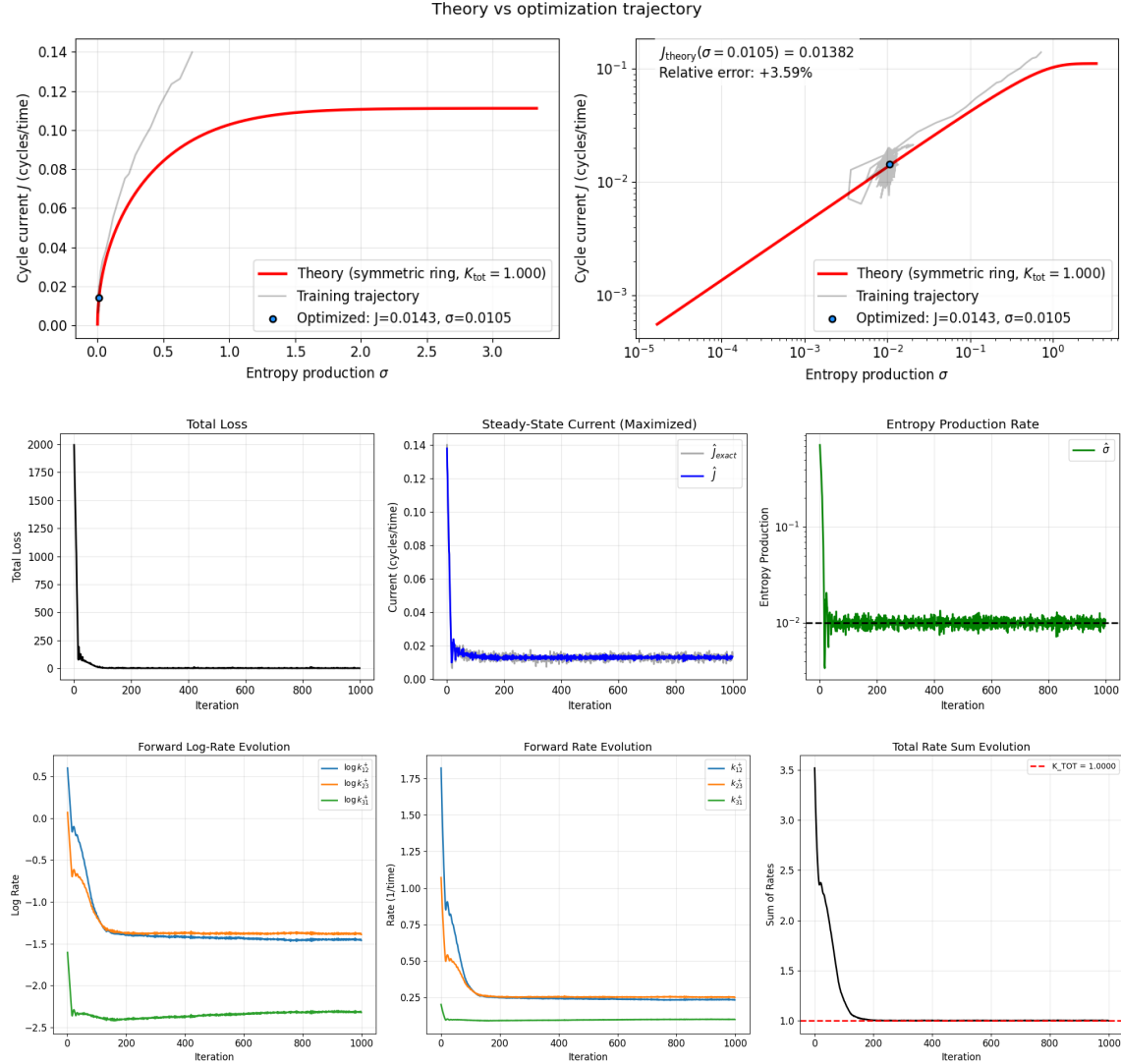


FIG. S10. **Optimization details for  $\sigma = 0.01$ .** **(Top)** Optimization trajectory in the current–dissipation plane; gray: training trajectory, blue: final point, red: theoretical Pareto front. **(Middle)** Training dynamics of total loss, steady-state current (gray: exact, blue: propensity-based estimate), and entropy production (dashed: target). **(Bottom)** Evolution of forward rates in log and linear scale, and total kinetic budget  $K_{\text{tot}}$  (dashed red: target).

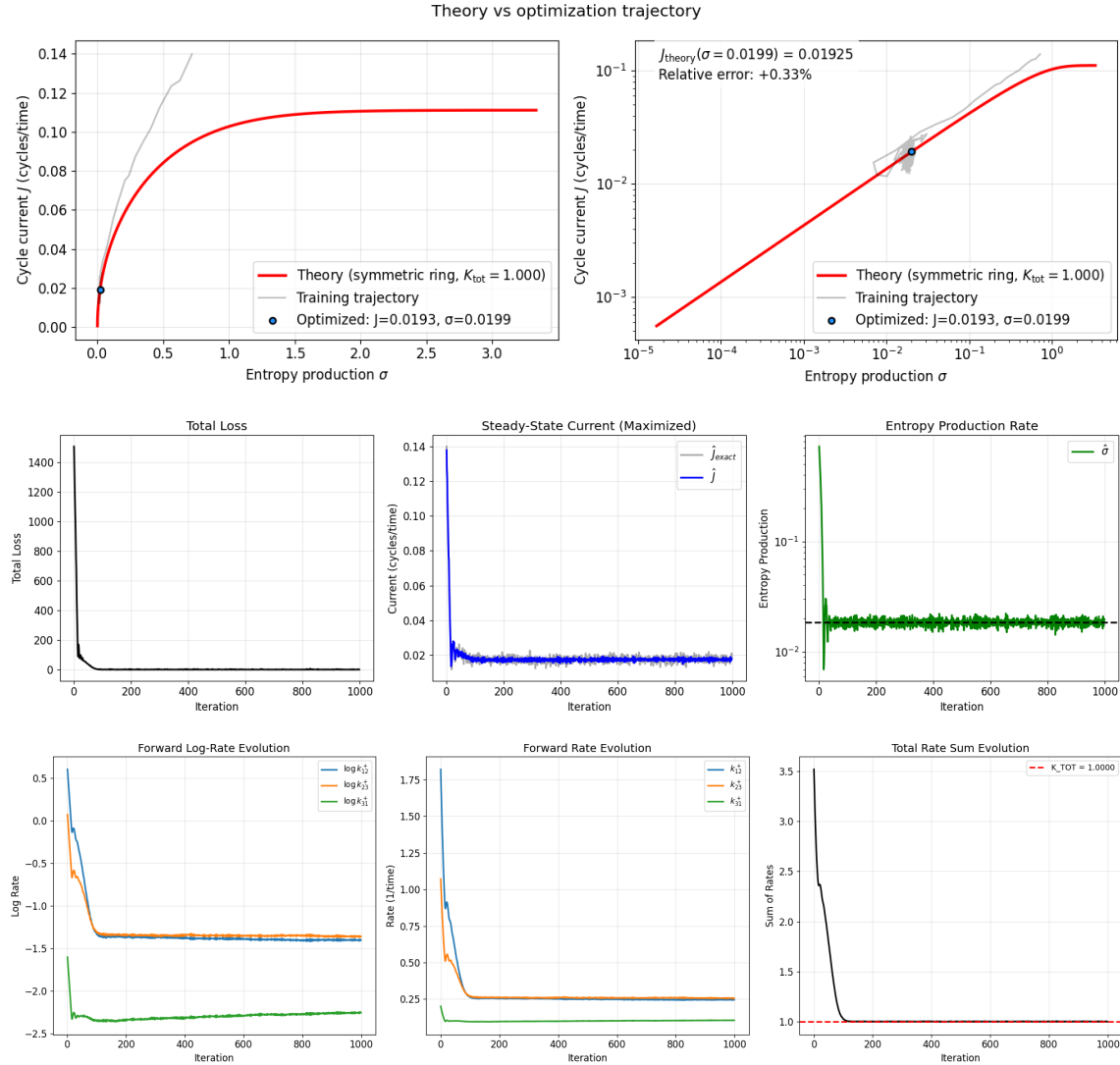


FIG. S11. Optimization details for  $\sigma = 0.018$ . Same format as Fig. S10.

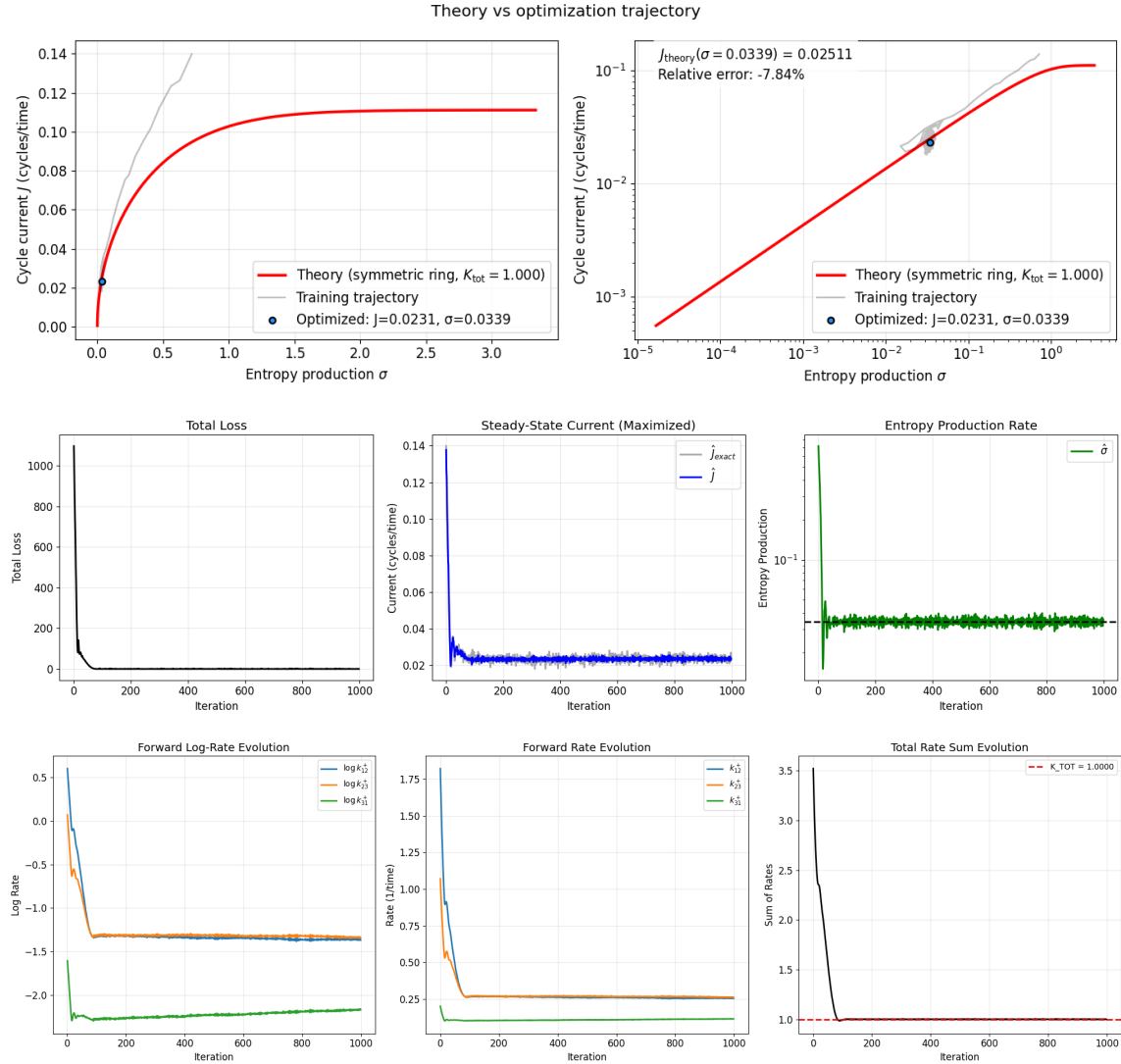


FIG. S12. Optimization details for  $\sigma = 0.034$ . Same format as Fig. S10.

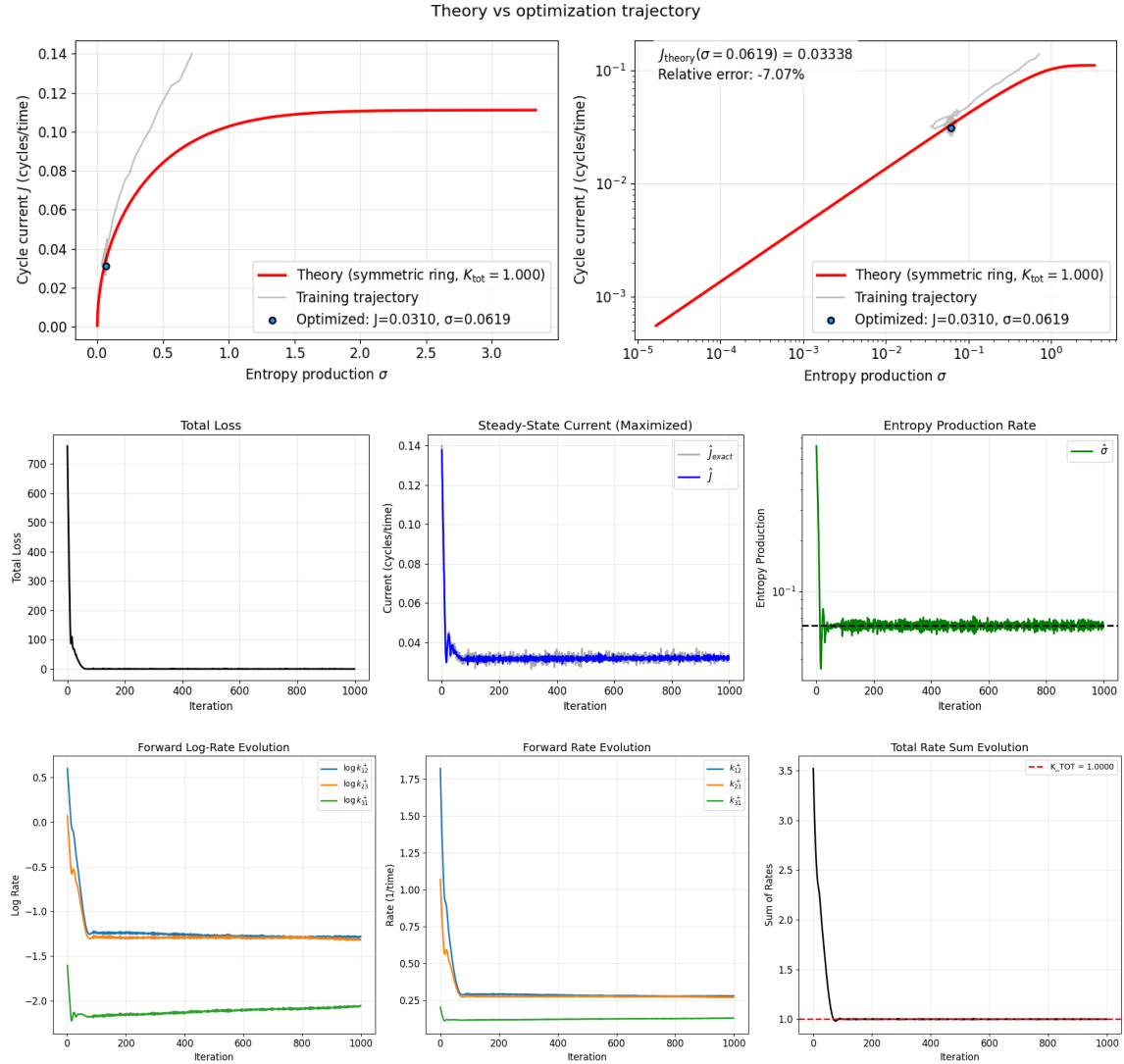


FIG. S13. Optimization details for  $\sigma = 0.063$ . Same format as Fig. S10.

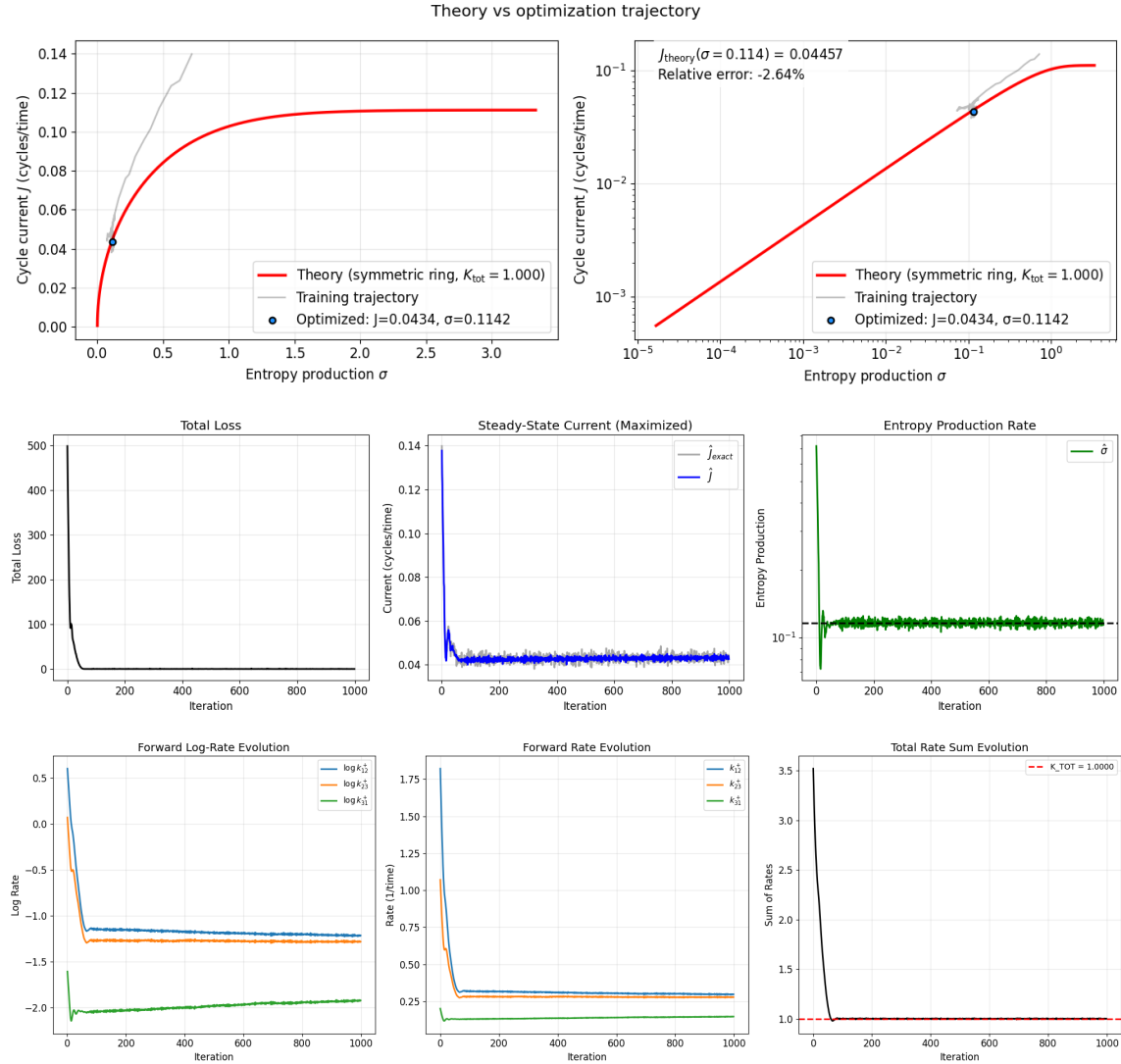


FIG. S14. Optimization details for  $\sigma = 0.12$ . Same format as Fig. S10.

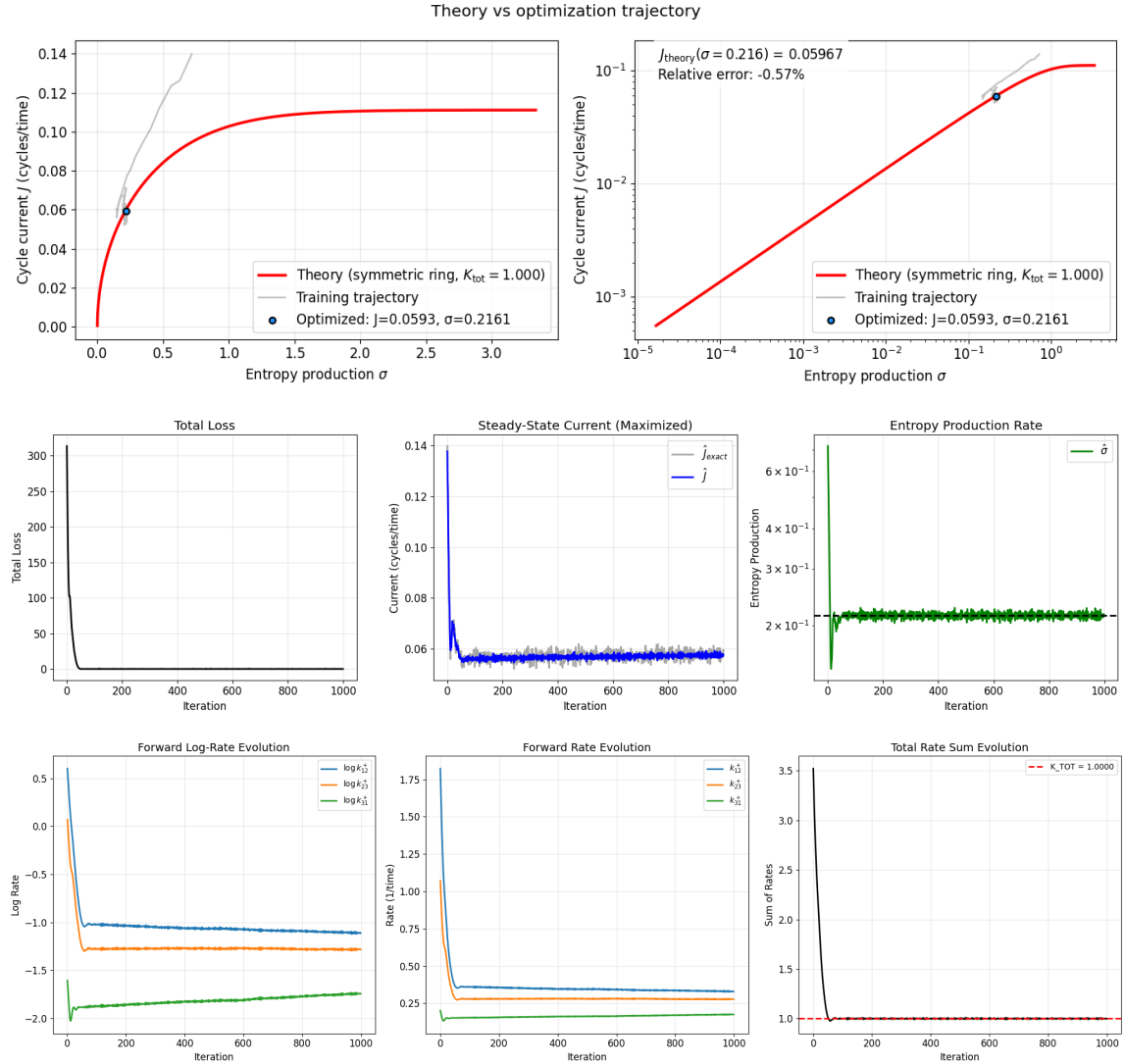


FIG. S15. Optimization details for  $\sigma = 0.21$ . Same format as Fig. S10.

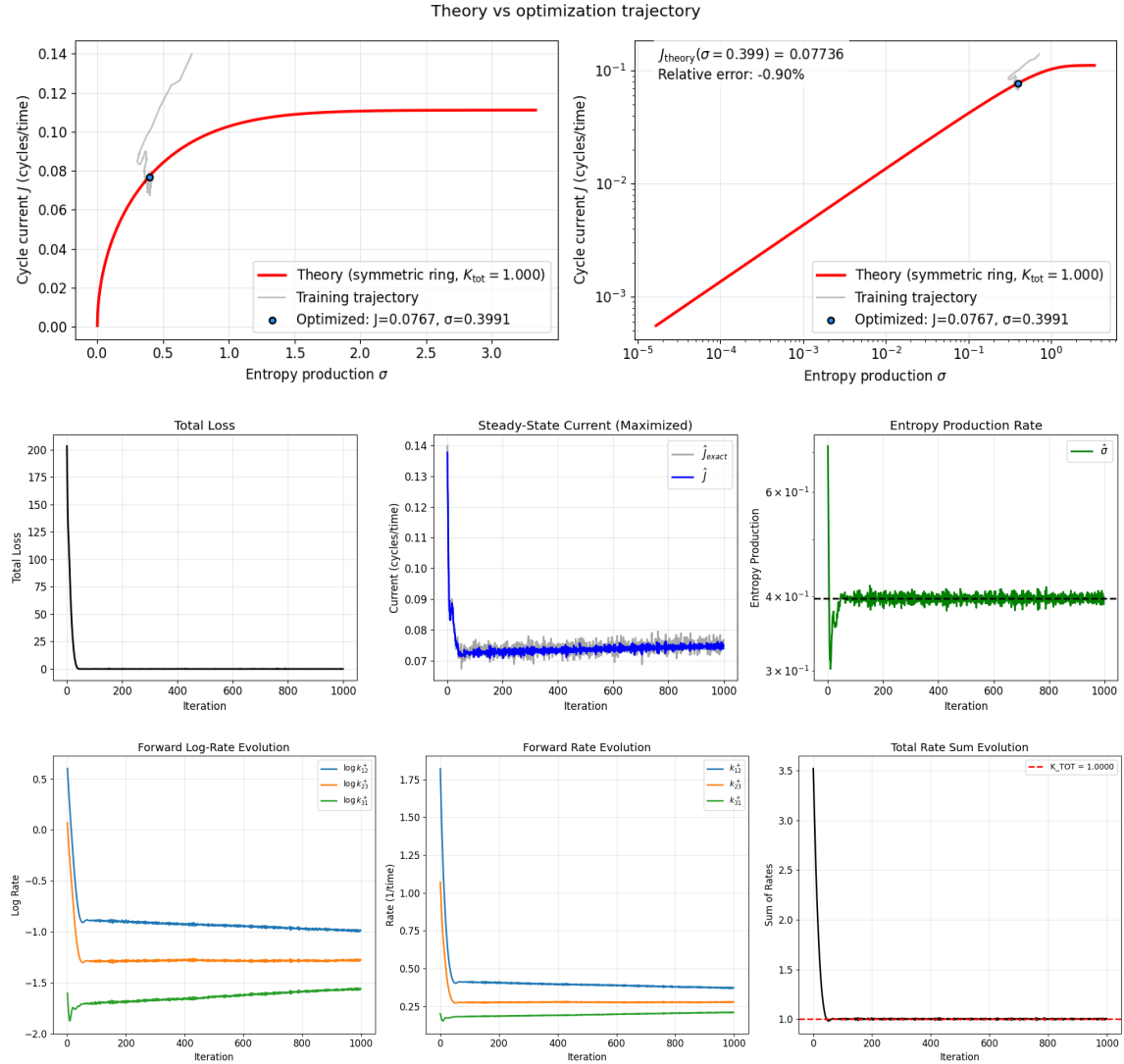


FIG. S16. **Optimization details for  $\sigma = 0.40$ .** Same format as Fig. S10.

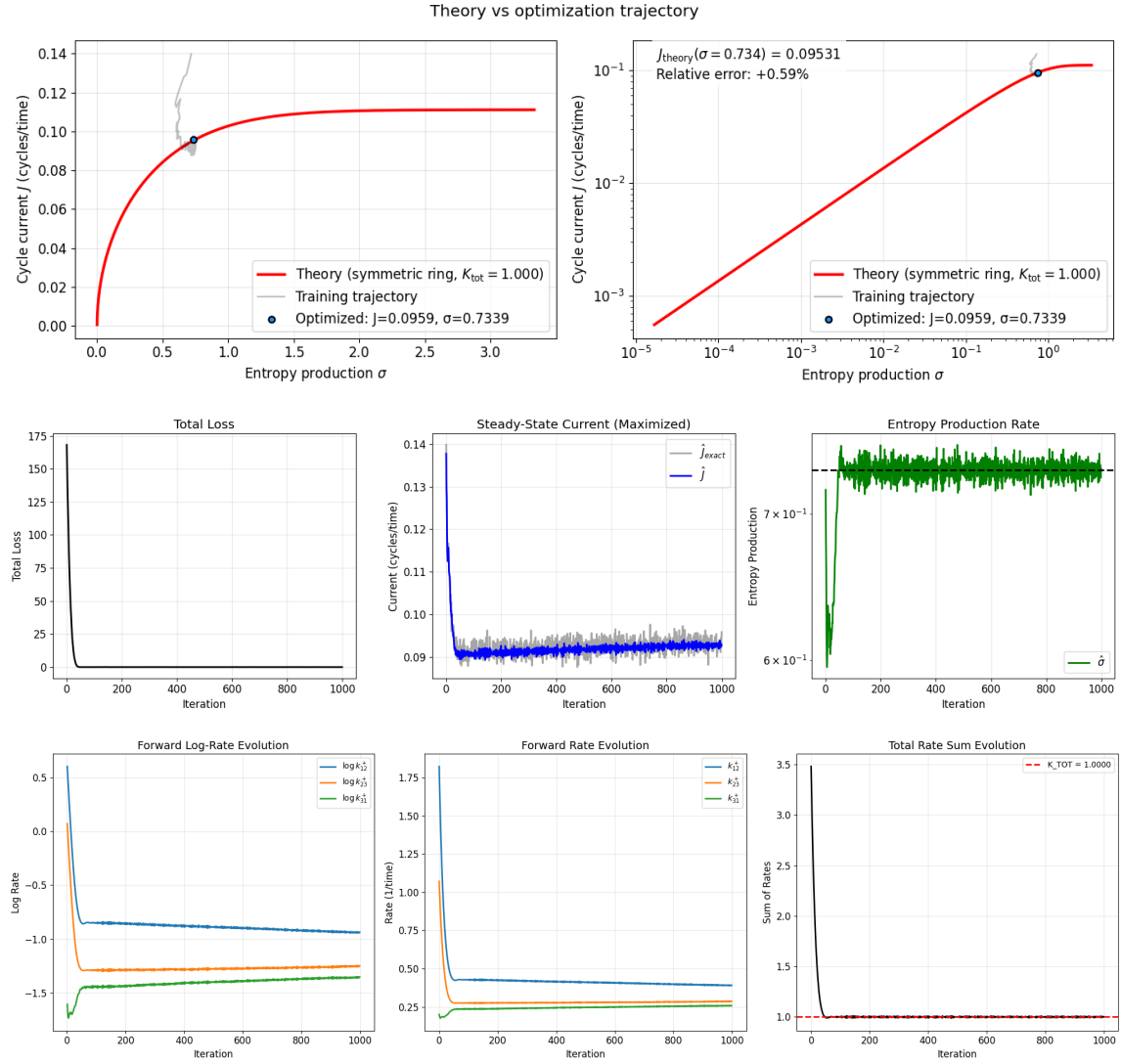


FIG. S17. **Optimization details for  $\sigma = 0.73$ .** Same format as Fig. S10.

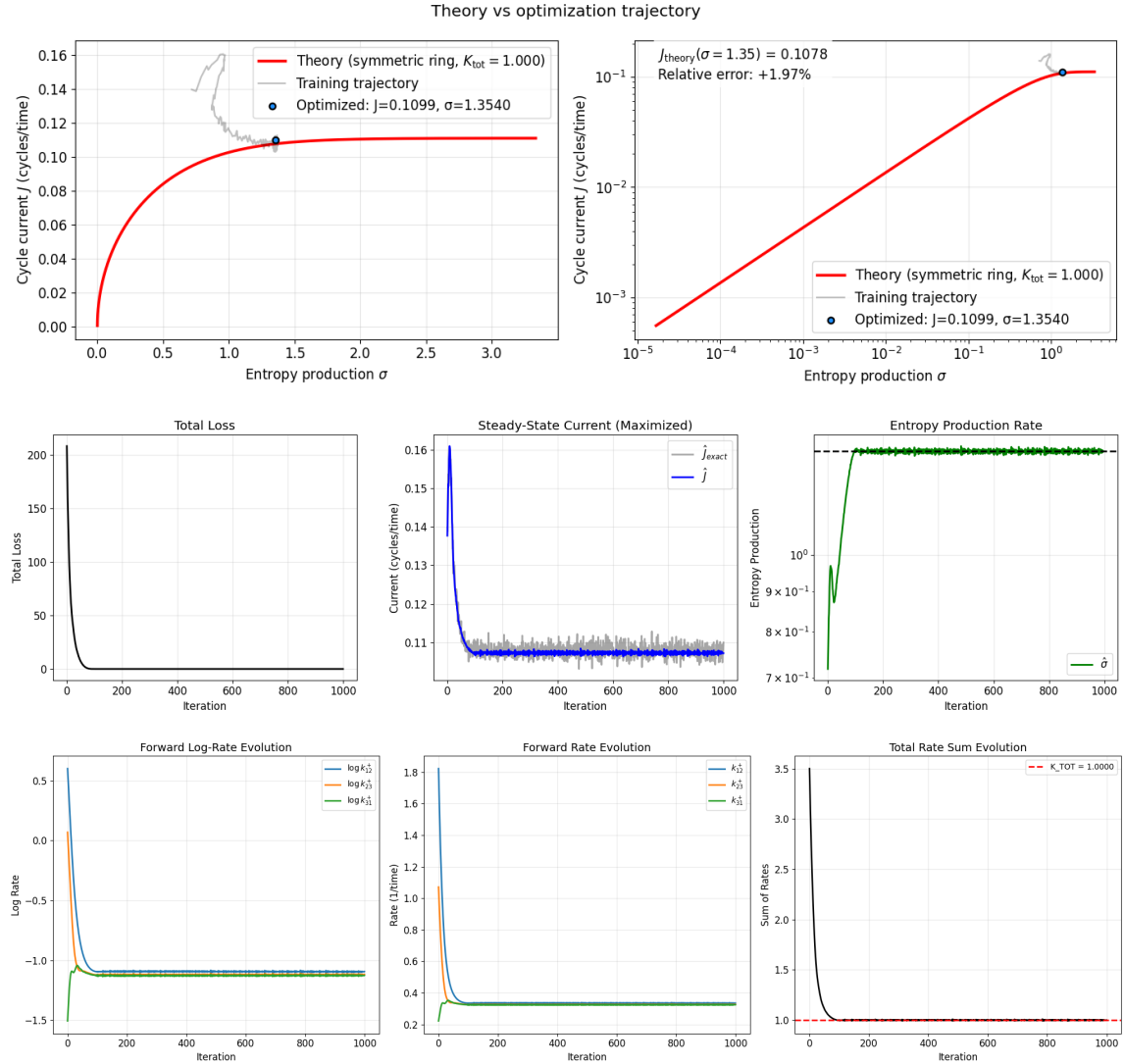


FIG. S18. Optimization details for  $\sigma = 1.35$ . Same format as Fig. S10.

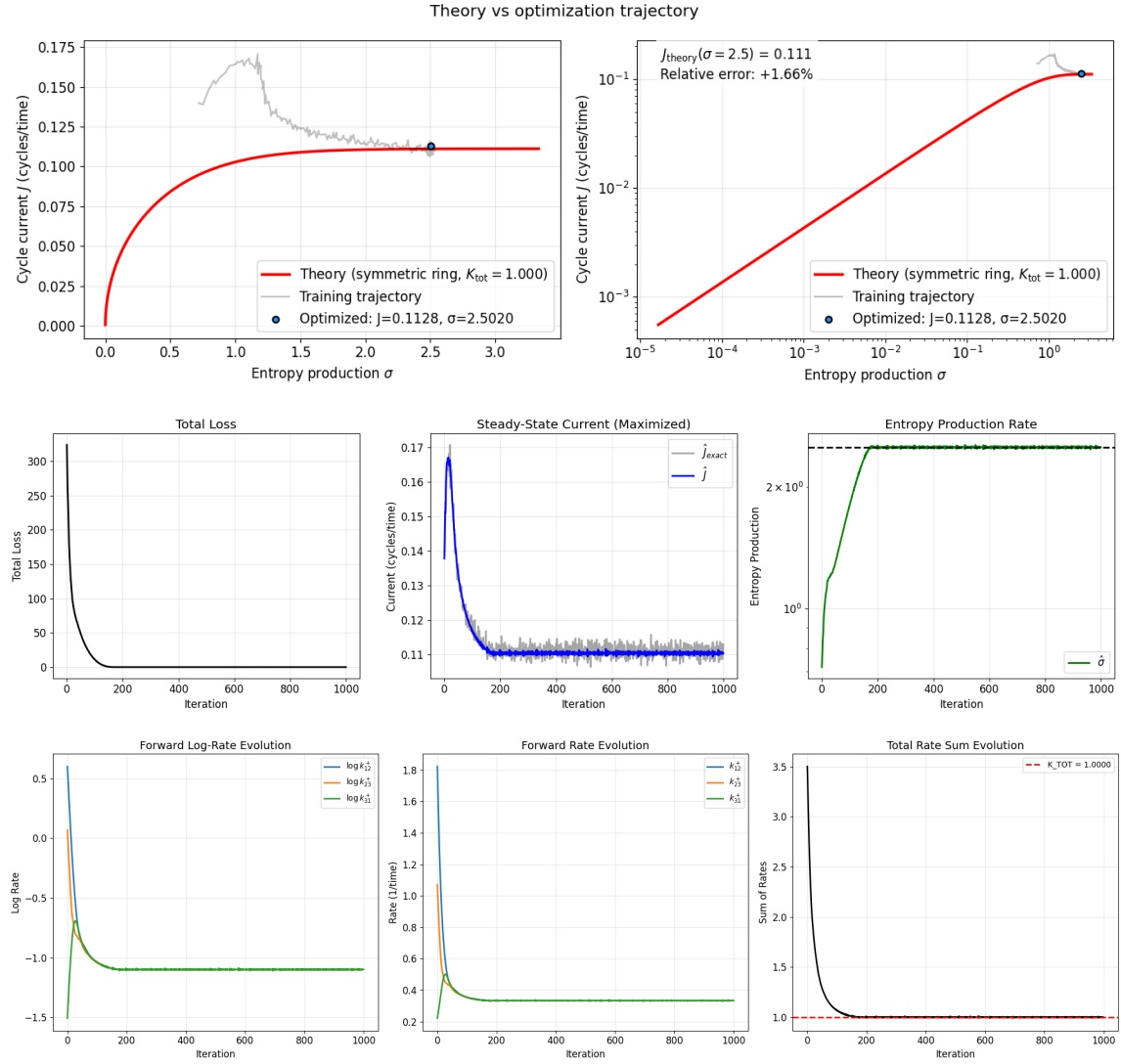


FIG. S19. Optimization details for  $\sigma = 2.5$ . Same format as Fig. S10.